POLITECNICO DI TORINO

Master of Science
in Mechanical Engineering

Master Thesis

Personal Thermal Management via Engineered Optical and Transport Phenomena

Supervisors

prof. Pietro Asinari
prof. Matteo Fasano
prof. Guido Raos

Candidate
Francesco Signorato

Academic year 2018/2019

Declaration of Authorship

I, Francesco SIGNORATO, declare that this thesis titled, “ Personal Thermal Management via Engineered Optical and Transport Phenomena” and the work presented in it are my own. I confirm that:

- This work was done wholly or mainly while in candidature for a research degree at this University.
- Where any part of this thesis has previously been submitted for a degree or any other qualification at this University or any other institution, this has been clearly stated.
- Where I have consulted the published work of others, this is always clearly attributed.
- Where I have quoted from the work of others, the source is always given. With the exception of such quotations, this thesis is entirely my own work.
- I have acknowledged all main sources of help.

Signed:

Date:

POLITECNICO DI TORINO

Abstract

Master of Science

Personal Thermal Management via Engineered Optical and Transport Phenomena

by Francesco SIGNORATO

The energy demand for cooling has nearly doubled in the last twenty years, namely the worldwide energy request went from 3.6 EJ in the years 2000 to 7 EJ in 2019. Recent studies reveal that if the efficiency in cooling technologies will not increase, then in the next twenty years the energy request will more than double due to the an higher human activity, urbanisation and climate change effects . Personal thermal management aims to control the local temperature of the body providing a sustainable cooling effect that can potentially save both energy and money. This work presents a numerical and experimental characterisation of both mass and heat transfer through smart polyethylene (PE) fabrics that exploit the simple structure of PE to guarantee both high transparency in the infrared region to enhance radiative heat transfer with the environment and visible opacity. Here, the performances of different PE fabrics are compared with conventional textiles (e.g. cotton) both in indoor and outdoor conditions. The higher cooling capacity that PE textiles demonstrate makes them a cheap and affordable solution to diminish the energy demand for air conditioning in a sustainable way.

Acknowledgements

This work is the result of my research at Massachusetts Institute of Technology and Politecnico di Torino. During the production of this work I had the opportunity to benefit from the help of different people, that I want here to acknowledge.

Firstly, I would like to thank all my supervisors, in particular prof. Pietro Asinari, prof. Matteo Fasano and prof Gang Chen and Dr. Svetlana V. Boriskina. Doing research at MIT was my dream since the high school: thanks to them my dream comes true. For this reason, I will never be grateful enough to you. Moreover, I want to thank all the multi-Scale ModeLing Laboratory at Politecnico, in particular Matteo Alberghini, Matteo Morciano and Luca Bergamasco for the precious suggestions and advice.

During these years of university I have known great friends that I want to thank all, I owe a particular recognition to Antonio that has always been with me and will continue to be there for my future life.

Finally, I want to thank my family for the constant support and for always been with me.

Contents

List of Figures

To my parents . . .

Chapter 1

Introduction

This chapter gives a general classification of personal thermal management technologies, with a focus on the latest discoveries on infrared transparent fabrics for sustainable cooling.

1.1 Personal Thermal Management

Personal cooling technologies aim to guarantee the human comfort for different environmental conditions. A unique definition of comfort is still not present in the literature, but the ASHRAE (American Society of Heating, Refrigerating and Air conditioning) gives a very general definition [1] that can be adopted for the scope of this work: "condition of mind which expresses satisfaction with the thermal environment". If referring to indoor comfort, in general this is guaranteed with air conditioning systems (AC) which require relatively large consumption of electric energy. The international Energy Agency (IEA) has estimated that the demand for cooling energy has increased from 3.6 EJ in 2000 to 7 EJ in 2019 [2], thus innovative technologies are pivotal to increase cooling efficiency and diminish the energy demand. At present, the most promising complementary solutions to AC systems are based on personal thermal management technologies which, rather than regulate the temperature of a whole environment, focus directly on the local regulation of the human body temperature.

1.2 Human Body Thermoregulation

The temperature of the human skin is the result of a energy balance between the body and the environment. In particular, when the heat is generated within the body by the metabolic rate M, it is spread over the whole body by blood circulation. Thus, the heat is transferred by the blood to the skin, namely the body surface, by conduction. Here, the clothes behave as resistance for heat, which is finally exchanged with the environment by convection C, radiation R, conduction K and evaporation of sweat E. The thermal equation of the body can be derived in different forms [3], but Yazdi proposes a more general definition that well describes the different contributions that affect the skin temperature [4]:

$$M - W = E + R + C + K + S$$

where W is the mechanical work performed by the body thanks to the metabolic rate M and S the heat storage, note that if the net gain of heat is null, then $S = 0$ and the body is in heat balance, on the contrary if $S > 0$ its tempearture will start to increase. The majority of the heat, nearly the 75%, is dissipated by radiation and convection, the rest mostly by evaporation, thus the properties of the clothes are pivotal to reach the most comfortable temperature for the skin, in general 37 ^{o}C, for different conditions of the environment.

1.3 Classification of Personal Cooling Systems

Personal cooling systems can be divided in three categories based on the different physics guiding the technology [4]:

- Air Cooled Garments (ACG): convection
- Liquid Cooled Garments (LCG): conduction
- Phase Change Garments (PCG): latent heat

In ACG, convection and evaporation are the two main sources of cooling: an external compressor, embedded in the fabric, forces cold air on it to increase the velocity of the flow thus enhancing the heat exchange. LCG present a network of small pipes and tubes under the fabric that spread a cold liquid, which in general is water, on the surface of the body. Once the liquid is heated up by the heat from the body, the fluid comes back into a refrigerating tool that cools down the fluid. Finally, PCG are based on the latent heat storage of phase change materials (PCM): the heat that the body produces is absorbed by the PCM, which typically is water or a paraffin. Specifically, when the temperature of the body increases, the heat is absorbed by the PCM in the liquid phase, then when the body temperature decreases again, the PCM solidifies and the heat is transferred back to the body.

All these technologies target in general cooling in extreme environments, like military applications, firefighters garments, or high performance clothes for professional athletes. Thus, all these solutions turn out to be very expensive and generally very bulky to be adopted by common users. For this reason, in 2014, a group of researchers from Massachusetts Institute of Technology (MIT) patented an innovative solution for personal cooling [5], which is based on radiative cooling (see section 2.4.2): "Infrared Transparent Visible Opaque Fabrics", (ITVOF). The goal of the this technology is to be applied to the whole population, not only to specific sectors of the textile industry. Moreover, since the latter is based on cheap recycled materials this could represent a low cost and sustainable solution to introduce in the market.

1.4 Polyethylene Fabrics

The ITVOF technology is completely passive [6], thus it does not require any sort of external energy source to guide the cooling process. Based on tailored optical properties of polyethylene, it enhances the radiative heat exchange with the environment thus increasing the comfort for the human body (see section 2.4).

The technology consists in making polyethylene fibers from recycled plastic with specific weaving parameters, i.e. diameter of the fibers or the distance between fibers. Besides having interesting optical properties, the use of polyethylene can guarantee other important advantages, in fact it allows to [7]:

- reduce the carbon footprint: the production of cotton requires infrastructures both for the growth and the cultivation management, thus enabling a huge demand for energy and large CO_2 emissions [8].

- reduce water consumption and pollution: the general procedure for dying clothes consists in immersing them in coloured water, then to wash them with hot water and re-immerse them in coloured water. The process is repeated several times until the colour is stable over the washing cycles. It has been estimated that 200 L of water are used the produce 1 kg of fabrics, thus increasing the water consumption and streams pollution during the discharging phase of the dyed water [7]. Both the production and colouring process of PE instead can be developed with alternative techniques, e.g. nano particles embedded in the fibers during the fabrication process for the colouring, that does not require the use of water.

FIGURE 1.1: Pollution of streams due to the dying process of common textiles. On the left the Nashua River (MA, USA), in which dyed water was poured, on the right the clean water after that a waste treatment system has been installed (Figure from [7]).

An issue linked to the use of polyethylene for garments is that PE does not present polar groups in its structure, thus it shows hydrophobic properties that clash with comfort requirements for human body. In fact, fabrics require hydrophilic properties so that the sweat produced by the human body can spread within the garment to enhance its evaporation. In the literature, PE is generally woven with hydrophilic material [9], e.g. cotton, to split the radiative contribution of comfort R and the evaporative one S between the hydrophobic PE and hydrophilic cotton, respectively [9].

1.5 Outline of the Research

This research has been carried out at Massachusetts Institute of Technology at the Mechanical engineering department in the Rohsenow Kendall Heat Transfer Laboratory under the supervision of Prof. Gang Chen and Dr. Svetlana V. Boriskina, who conceived the idea of smart polyethylene for personal thermal management [6]. Specifically, this work aims to deepen the following topics, which in the document will be called **T1**, **T2**, **T3**:

T1. Gain a better understanding about the surface chemistry of polyethylene fabrics and their hydrophilicity (see section 4.2).

T2. Experimentally characterise the water transport properties of different types of textiles and create a mathematical model that is able to predict the sweat motion within the clothes (see section 4.3).

T3. Experimentally characterise the thermal performances of different textiles on the human body both in indoor and outdoor conditions. (see section 4.4).

To do so, *Chapter* 2 gives an insight on the interaction between light and matter, with a specific focus on thermal radiation. In addition, it presents the experimental set up that has been used to test the thermal performances of the ITVOF technology. *Chapter* 3 introduces the mathematical formulation and the experimental methods to account for the spread of water (which mimics human sweat) within the fabric. Finally, *Chapter* 4 presents the main results of the activity that are then summarised in *Chapter* 5.

Chapter 2

Absorption and Scattering of Light

The main physics involved in the study of polyethylene fabrics cooling capacity are:

- interaction between matter and light, in particular thermal radiation, that allows to describe the different responses of the fabric when it is exposed to waves with different wavelengths.
- water mass transport through porous media, that describes both the spread of sweat in the garment and the evaporation rate towards the environment.

This chapter address the first topic. Note that the study of the interaction between light and matter is a broad topic, within this section only the interactions between light and small particles will be proposed in the framework of the Maxwell's equations. Instead, a quantum mechanic approach is out of the scope of this work.

2.1 Basic Theory of Scattering and Absorption

Matter is constituted by atoms which are in turn made of charged subatomic particles, namely electrons and protons. When atoms are hit by electromagnetic waves, charged subatomic particles start to oscillate because of the electric field of the external radiation. The latter oscillations emit in turn electromagnetic waves in all the space directions: this second emission is called "*scattering*". Moreover, when illuminated by waves the electrical charges can transform part of the electromagnetic energy in thermal energy: this is called "*absorption*". Absorption is linked to the natural vibrational modes of the electrons, thus when the external frequency of the wave is equal to the natural frequency of the charged subatomic particles these one will absorb energy by converting the vibrational energy into thermal one. The equivalent of this process in vibration mechanics is the classical mass-spring system which when excited to its natural frequency present the maximum frequency response, thus the maximum oscillation possible. Similarly, electrons excited to their natural frequency can be imagined to show bigger oscillations, that due to impacts with other electrons, are transformed into thermal energy.

2.2 Basics of Classic Propagation Theory

In the literature there are three different models to approach the description of solid state physics [10]:

- Classic
- Semi Classic

- Fully Quantum

This work focuses on the first, since the light is described as an electromagnetic wave governed by Maxwell's equations and the medium, namely the matter, as a dipole oscillator. In the second approach, the atom is described through quantum mechanics, but the light still with a wave description. Finally, the third theory relies on quantum mechanics both for the light and the medium. Below, an introduction to Maxwell's equations and the dipole oscillator model are proposed, since they constitute the basis of classic propagation theory.

2.2.1 Notions of Electromagnetism

The physical framework in which scattering and absorption can be described is the electromagnetic theory. The fundamental equations to deal with those problems are the Maxwell's equations, whose expressions for a macroscopic field are reported below [11]:

$$\nabla \cdot D = \rho_f \tag{2.1}$$

$$\nabla \cdot B = 0 \tag{2.2}$$

$$\nabla \times E + \frac{\partial B}{\partial t} = 0 \tag{2.3}$$

$$\nabla \times H = J_F + \frac{\partial D}{\partial t} \tag{2.4}$$

E is the electric field, B the magnetic induction and J_F, ρ_F are the current and charge density, respectively. The electric displacement D and the magnetic field H can be computed as:

$$D = \epsilon_0 E + P \tag{2.5}$$

$$H = \frac{B}{\mu_0} - M \tag{2.6}$$

where μ_0 and ϵ_0 are the permeability and dielectric constant of void respectively, while P is the polarization and M the magnetization. In addition, also the constitutive equations must be considered:

$$J_F = \sigma E \tag{2.7}$$

$$B = \mu H \tag{2.8}$$

$$P = \epsilon_0 \chi E \tag{2.9}$$

where σ, μ and χ are the conductivity, permeability and susceptibility of the medium. To keep a general approach, instead of considering an harmonic electromagnetic field that can not be always the case, Maxwell's equations are analysed by Fourier transform as follows (considering null charge density ρ_F):

$$\nabla \cdot D(\omega) = 0 \tag{2.10}$$

$$\nabla \cdot B(\omega) = 0 \tag{2.11}$$

$$\nabla \times E(\omega) = i\omega B(\omega) \tag{2.12}$$

$$\nabla \times H = J_F(\omega) - i\omega D(\omega) \tag{2.13}$$

where ω is the frequency of the wave. Obviously, the Fourier transform is applied also to the constitutive equations:

$$J_F(\omega) = \sigma E(\omega) \tag{2.14}$$

$$B(\omega) = \mu H(\omega) \tag{2.15}$$

$$P(\omega) = \epsilon_0 \chi E(\omega) \tag{2.16}$$

An other important quantity for the analysis of scattering and absorption is the so called Poynting Vector, which describes the amount of energy transferred per unit of surface and unit of time by the electromagnetic wave. Given the electric field E and magnetic field H, the Poynting vector is defined as:

$$S = E \times H \tag{2.17}$$

In general, since the instantaneous Poynting vector is difficult to measure, a time averaged quantity is more common. In addition, if one considers electric and magnetic fields to be harmonic, the time averaged Poynting vector reduces to:

$$\bar{S} = \frac{1}{2} Re(E_c \times H_c^*) \tag{2.18}$$

where E_c and H_c are the complex functions related to the harmonic wave. The modulus of the Poynting vector is called irradiance and has the measure unit of $Wm^{-2}s^{-1}$. The last property to label a wave is the so called "polarization". The polarization plane is the one that contains the electric field and the direction of propagation of the wave; the vibration plane, on the contrary, is the one containing the magnetic field and the direction of propagation. Three types of polarization can be identified: linear, circular and elliptic. A wave is said to be linearly polarized when the direction of oscillation of the electric field is fixed in time: in that case vertical and horizontal polarization are possible. When the oscillation of the electric field rotates along the direction of propagation, the wave in general is elliptically polarized; in the particular case in which the semi axis of the ellipse are equal, the wave is circularly polarized. In the most general case of elliptic polarization, other key parameters must be defined:

- Handedness: describes the sense of rotation of the ellipse, namely right or left handed. The most common notation is to define a right handed elliptically polarized wave the one in which the oscillation ellipse is clockwise with respect to an observer that is looking the wave approaching him.
- Ellipticity: ratio of the semi axis of the ellipse.
- Azimuth: angle defined by the major axis and a conventional direction.

These three parameters and the irradiance are the so called "ellipsometric parameters" and fully describe a wave of a given frequency.

2.2.2 Hypothesis of the Dipole Model

The dipole model gives a description of the medium in which light propagates and interacts. According to this classical model, there are three different types of oscillators into the matter, each with its proper resonant frequency [10]:

- atomic oscillators

- vibrational oscillators
- free electron oscillators

Atomic oscillators

In the oscillator model, the atom is described from a mechanical perspective as if the nucleus is connected through a spring to its electrons. Thus, the spring represents the attraction force between a positive nucleus and a negatively charged electron, being described through an elastic constant K_s. The presence of a positive and a negative charge generates an electric dipole, whose intensity depends on constant K_s. In addition, an equivalent mass can be introduced if one consider the *reduced mass* μ:

$$\frac{1}{\mu} = \frac{1}{m_e} + \frac{1}{m_N} \tag{2.19}$$

where m_e and m_N are the mass of the electron and the nucleus, respectively. Under this perspective, the "mechanical" dipole has a resonant frequency that can be computed as:

$$\omega_0 = \sqrt{\frac{K_s}{\mu}} \tag{2.20}$$

that represents the dipole oscillations due to the presence of bound electrons within the atom. It naturally follows that each atom can have more than one resonance frequency, as also experimentally seen by emission and absorption spectra. At equilibrium, the dipole oscillates by emitting waves at their resonant frequencies. The oscillations of the dipole are mainly due to the movement of electrons $x(t)$. In fact, the nucleus, which is heavier, tends to be stationary, thus the oscillations of electrons produces themselves a time dependent dipole moment:

$$p(t) = -e \cdot x(t) \tag{2.21}$$

Based on this, when an atom interacts with an external wave with frequency ω, two alternative scenarios are possible:

- if the external frequency ω is equal to the resonant frequency ω_0, then the atom oscillates at resonance with larger oscillations and it absorbs energy from the external wave, whose decay can be described through Beer's model:

  $$I(x) = I_0 e^{-kx} \tag{2.22}$$

  where I_0 is the intensity of the wave before interacting with the medium at $x = 0$ and k the attenuation coefficient.

- if the frequency ω is different from the resonance one, the atom will be transparent to the incoming wave, without absorbing it. In that case, as it happens in purely mechanical vibrating systems, the atom oscillates with the same frequency of the external field but with a phase difference, which translates in a different velocity of the outgoing wave as described by the refractive index:

  $$n = \frac{c}{v} \tag{2.23}$$

  where c is the light speed and v the speed of the outgoing wave.

Vibrational oscillators

In addition to atomic oscillators, namely dipoles that are present within the atom, also vibrational oscillators can be introduced if considering a compound, for example a ionic compound, e.g. salt. In this case the bound electrons are closer to the Cl atom than to Na ones, thus if considering the whole lattice instead of the single atom, also in this case a dipole is present.
These oscillations present lower frequencies as can be noticed in equation 2.20, due to an higher reduced mass. For this reason, in general, absorption peaks due to vibrational oscillators are common in the infrared region $10^{12} - 10^{13} Hz$ rather than at $10^{14} - 10^{15} Hz$, as for atomic oscillators. In the case of external waves with frequency ω that interact with these compound, the same considerations that have been described for atomic oscillators are valid.

Free electron oscillators

The above mentioned oscillators are based on bounded electrons, but if considering metals or other materials, there can also be electrons that are free and not bounded. In that case, the force between free electrons and the nucleus is zero, since it can be imagined that K_s elasticity constant of the spring is null. Thus, in this case, the resonant frequency for free electron oscillators is $\omega_0 = 0$

2.2.3 Frequency Dependent Absorption coefficient

Knowing the hypothesis on which is based the dipole model, it is cumbersome to show how the absorption of the medium strongly depends on the frequency of the incident wave.
As an example, here a single atom with a unique resonant frequency ω_0 is considered. The interaction of the wave with the atom is described exactly as a mechanical vibrating system, namely as damped single degree of freedom (SDOF) that undergoes an external harmonic force of frequency ω [10]. In this case, a single degree of freedom is sufficient, since the nucleus mass is considered much greater than the one of the electron, thus the oscillations of the nucleus are neglected. The equation of motion for a SDOF system is:

$$m\frac{d^2x}{dt^2} + m\gamma\frac{dx}{dt} + m\omega_0^2 = F(t) \tag{2.24}$$

where F(t) is the external harmonic force, γ is the damping coefficient, m the mass of the system and ω_0 its natural frequency. In the case of a electromagnetic problem, the latter equation can be re-written for the mass of electron m_e as:

$$m_e\frac{d^2x}{dt^2} + m_e\gamma\frac{dx}{dt} + m_e\omega_0^2 = -eE(t) \tag{2.25}$$

where $E(t)$ is the external electric field and e is the charge of the electron.
Supposing that $E(t)$ has the form:

$$E(t) = E_0 exp(i\omega t), \tag{2.26}$$

then the response of the system $x(t)$ has the same form of the external field with the same frequency but a phase shift ϕ:

$$x(t) = X_0 exp(i\omega t - \phi), \tag{2.27}$$

where $X_0 \in C$ is the amplitude of the response. By substituting equation 2.27 in equation 2.25 and doing some simple algebra, the final expression of X_0 can be computed as a function of the external frequency ω:

$$X_0 = \frac{-e\frac{E_0}{m_e}}{\omega_0^2 - \omega^2 - i\gamma\omega} \tag{2.28}$$

It follows that only if the external field has a frequency similar to the natural frequency of the system the oscillations of the electrons turn out to be large (Figure 2.1), in all the other cases they have a reduced intensity depending on the damping factor, which in the case of electromagnetic problem represents the possible collision with phonons.

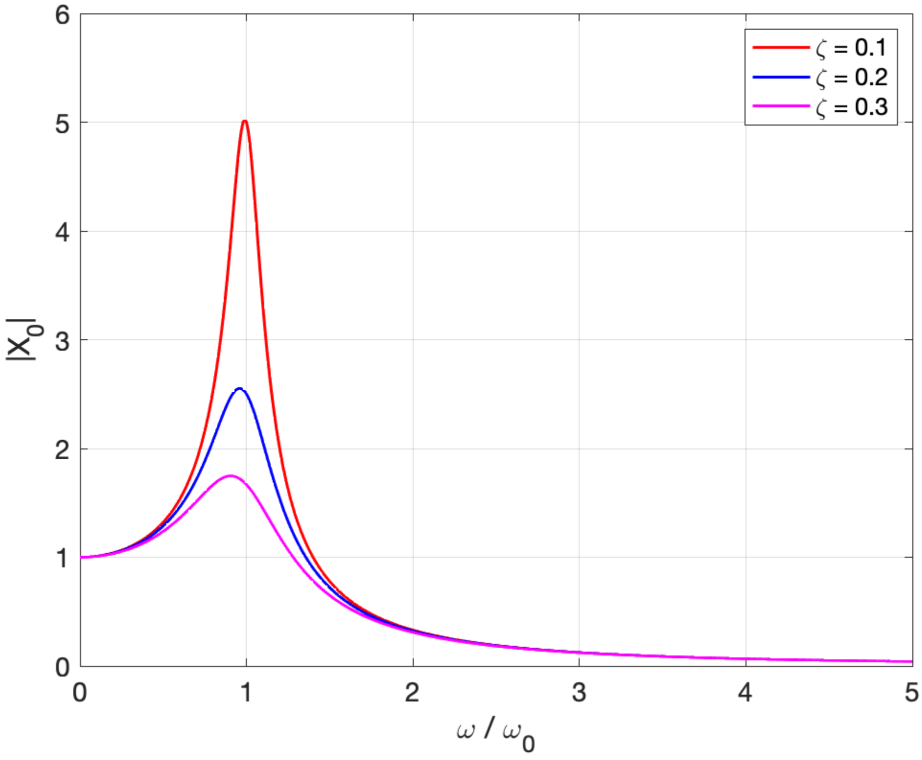

FIGURE 2.1: Absolute value of the response X_0 as a function of the frequency of the external field ω for different value of damping $\zeta = \zeta(\gamma)$

The movement of atom X_0 generates a dipole moment which varies in time as described by equation 2.21. If considering a number N of atoms, then the "macroscopic polarization" P_{res}, namely the dipole moment per unit volume can be expressed as:

$$P_{res} = N \cdot p = -N \cdot e \cdot x(t) = \frac{Ne^2}{m_e} \frac{E_0}{(\omega_0^2 - \omega^2 - i\gamma\omega)} \tag{2.29}$$

Based on equations 2.5 and 2.16, the electric displacement becomes:

$$D = \epsilon_0 E + \epsilon_0 \chi E + P_{res} \tag{2.30}$$

and under the assumption of isotropic material, D can also be expressed as:

$$D = \epsilon_0 \epsilon_r E, \tag{2.31}$$

where ϵ_r is the relative dielectric constant. By equating equations 2.30 and 2.31, then ϵ_r can be extracted:

$$\epsilon_r(\omega) = 1 + \chi + \frac{Ne^2}{m_e} \frac{E_0}{(\omega_0^2 - \omega^2 - i\gamma\omega)}, \tag{2.32}$$

where the real and imaginary components are:

$$\epsilon_{real}(\omega) = 1 + \chi + \frac{Ne^2}{m_e \epsilon_0} \frac{\omega_0^2 - \omega^2}{(\omega_0^2 - \omega^2)^2 + (\gamma\omega)^2} \tag{2.33}$$

$$\epsilon_{imag}(\omega) = \frac{Ne^2}{m_e \epsilon_0} \frac{\gamma\omega}{(\omega_0^2 - \omega^2)^2 + (\gamma\omega)^2} \tag{2.34}$$

Experimental studies [10] show that the absorption coefficient α is related to the imaginary part of the dielctric constant $\epsilon_{imag}(\omega)$:

$$\alpha(\omega) \Longleftrightarrow \epsilon_{imag}(\omega) \tag{2.35}$$

which confirms the different absorption peaks of the matter as a function of the frequency ω of the incident radiation.

2.3 Scattering and Absorption by Arbitrary Small Particles

In general, in absorption and scattering problems, also the cross sectional area is employed to describe the interaction light - particle, to give a sense of the specific amount of energy that is absorbed or scattered. To introduce this quantity, a simple example of Maxwell's equation solution is proposed [11].

In this problem a given particle of a given shape, material and refractive index is illuminated by an incident electromagnetic wave E_i, H_i; we want to calculate the electric and magnetic field both in the surrounding E_2, H_2 and within the particle E_1, H_1 (Figure 2.2) . The solution to this type of problem is obtained by solving the Maxwell's equations; in this section the case of an arbitrary particle shape is proposed. In the following analysis, the hypothesis that the incident field can be Fourier transformed in the series of plane monochromatic waves holds. If so, the simpler case of plane monochromatic incident field can be considered:

$$E_i = E_0 e^{i(kx - \omega t)} \tag{2.36}$$

where ω is the angular frequency, k the wave number $k = \frac{2\pi}{\lambda}$ and λ the wavelength. The electric field in the surrounding can be written as the sum of the scattered and the incident one:

$$E_2 = E_s + E_i \tag{2.37}$$

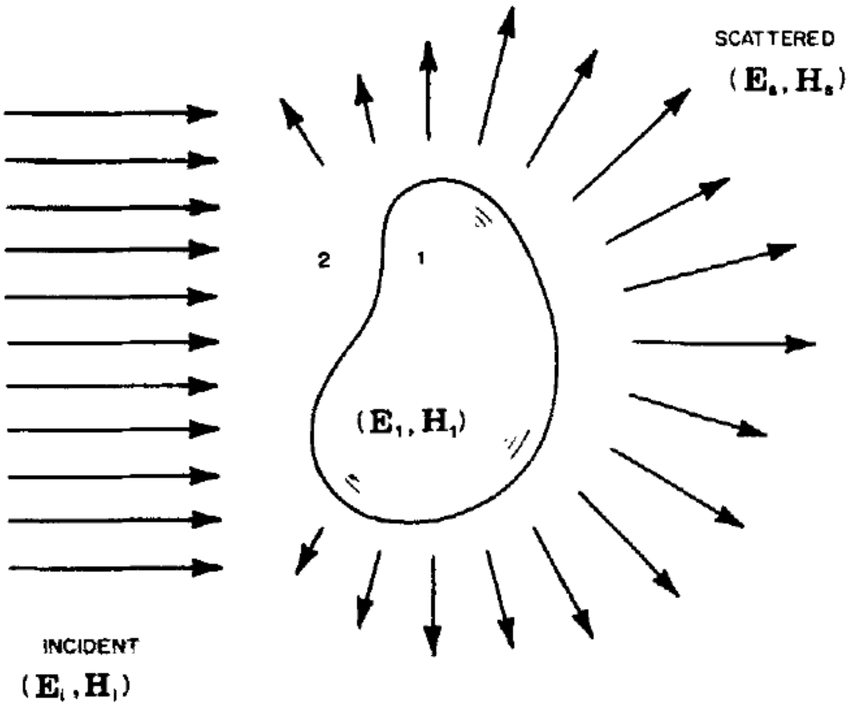

FIGURE 2.2: The incident electromagnetic wave E_i, H_i illuminates a particle of given shape, material and optical properties. The dipole oscillations within the particle cause both the scattered field E_s, H_s in the surrounding and the field within the particle E_1, H_1 (Figure from [11]).

Remembering equations 2.12 and 2.15, it is possible to obtain that:

$$\nabla \times (\nabla \times E) = i\omega\mu\nabla \times H \tag{2.38}$$

and by applying equation 2.5:

$$\nabla \times (\nabla \times E) = \omega^2\mu\epsilon E \tag{2.39}$$

where the curl of a curl is:

$$\nabla \times (\nabla \times E) = \nabla(\nabla \cdot E) - \nabla \cdot (\nabla E) \tag{2.40}$$

By combining equations 2.40 and 2.39, the vector wave equation can be obtained:

$$\nabla^2 E + k^2 E = 0 \tag{2.41}$$

where $k^2 = \omega^2\mu\epsilon$. Thus, an admissible solution is a electric field that satisfies the vector wave equation and is divergence free; the corresponding magnetic field can be calculated by equation 2.12. Now that the equation to solve has been obtained (see equation 2.41), the proper boundary conditions must be set. Discontinuities are present in the domain, in particular at the interface between the particle and the medium, thus here the conservation of energy must be guaranteed. To do so, it is possible to demonstrate [11] that it is sufficient to impose the equality between the tangential component of both electric and magnetic field in the medium and in the particle:

$$(E_2(x) - E_1(x)) \times n = 0 \tag{2.42}$$

$$(H_2(x) - H_1(x)) \times n = 0 \tag{2.43}$$

Once that also the boundary conditions are set, the problem is fully defined:

$$\begin{cases} \nabla^2 E + k^2 E = 0 \\ \nabla^2 H + k^2 H = 0 \\ (E_2(x) - E_1(x)) \times n = 0 \\ (H_2(x) - H_1(x)) \times n = 0 \end{cases} \tag{2.44}$$

The assumption to perform Fourier analysis of the incident wave allows to compute the solution as the superposition of the fundamental frequency by using the linearity of the aforementioned problem 2.44. In particular, the solution of an arbitrary polarized wave can be obtained thanks to the superposition of linearly polarized waves. The solution of the problem is space dependent, thus let us fix a local reference frame x,y,z in the centre of the particle and imagine to compute the solution along the scattering direction e_r which is inclined of the azimuthal angle ϕ with respect to the incident direction z and of the scattering angle θ with respect to the x axis (Figure 2.3).

The z direction, namely the direction of the incident radiation, is called *forward direction* and with the scattering direction r forms the *scattering plane* τ. The incident electric field E_i lays in the plane x-y, since it is perpendicular to the direction of propagation, and can be decomposed in two directions:

- $e_{\parallel,i}$, parallel to the scattering plane

$$E_{\parallel i} = cos(\phi)E_{xi} + sin(\phi)E_{yi} \tag{2.45}$$

- $e_{\perp,i}$, perpendicular to the scattering plane

$$E_{\perp i} = sin(\phi)E_{xi} - cos(\phi)E_{yi} \tag{2.46}$$

In the far region condition, that is far enough from the origin, the scattered electric field is supposed to be transverse ($\vec{e_r} \cdot \vec{E_s} = 0$) and can be computed as:

$$\vec{E_s} = \frac{e^{ik\vec{r}}}{-ikr} A \tag{2.47}$$

thus it can be decomposed as following:

$$\vec{E_s} = E_{\parallel s}\vec{e_{\parallel s}} + E_{\perp s}\vec{e_{\perp s}} \tag{2.48}$$

By remembering the linearity of the problem, the solution can be written as linear function of the incident wave:

$$\begin{bmatrix} E_{\parallel s} \\ E_{\perp s} \end{bmatrix} = \frac{e^{ik(r-z)}}{-ikr} \begin{bmatrix} S_2 & S_3 \\ S_4 & S_1 \end{bmatrix} \begin{bmatrix} E_{\parallel i} \\ E_{\perp i} \end{bmatrix} \tag{2.49}$$

where the elements of the scattering matrix S are in general complex functions of the scattering angle and azimuthal one. This procedure has shown how the solution for

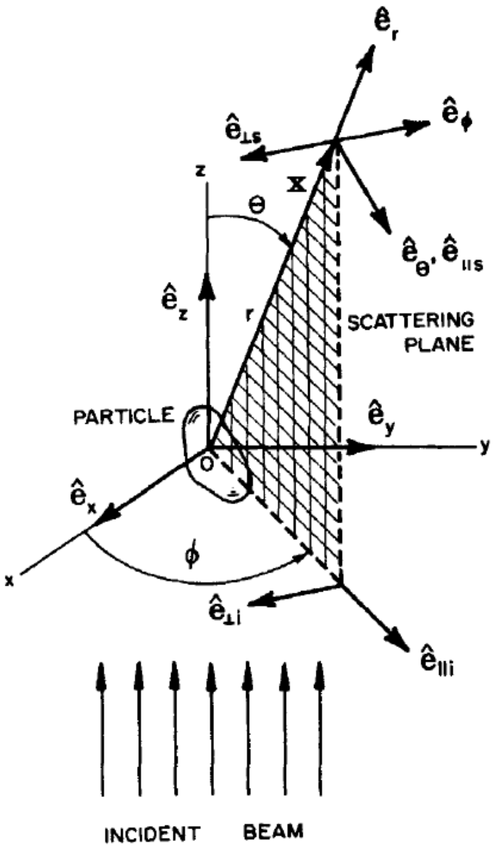

FIGURE 2.3: Solution of the Maxwell problem along the scattering direction r. The local reference system x,y,z is placed in the centre of each particle (Figure from [11]).

the scattered field is in general computed in scattering problem for a monochromatic plane incident wave.
To compute the absorbed field, an energetic approach is easier to be implemented: imagine to illuminate the particle and place a detector of area A behind it, in that case the extinction energy, namely the one that the detector can not measure due to the presence of the particle, is equal to the sum of both the absorbed energy and the scattered one (Figure 2.4). Thus, the extinction energy can be computed as:

$$W_{ext} = W_a + W_s \tag{2.50}$$

where:

$$W_{ext} = -\int S_{ext} \cdot \vec{e_r} dA \tag{2.51}$$

$$W_s = \int S_s \cdot \vec{e_r} dA \tag{2.52}$$

$$W_a = -\int S_a \cdot \vec{e_r} dA \tag{2.53}$$

where S_{ext}, S_s and S_a are the extinction, absorbed and scattered Poynting vector, respectively.

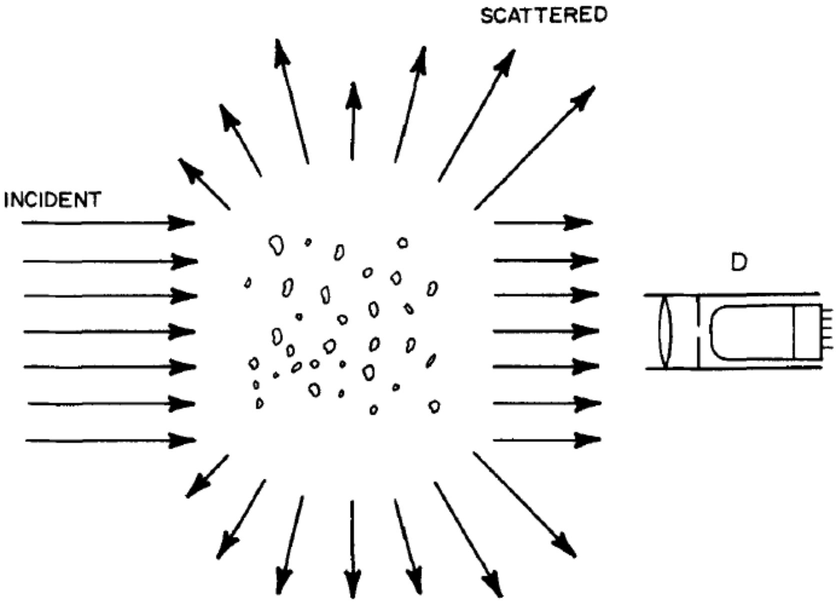

FIGURE 2.4: A detector of area A is placed behind the illuminated particle, the energy that the detector can not measured, namely the extinction energy is the sum of both the scattered and the absorbed one (Figure from [11]).

Knowing the solution for the scattered field, the energy transfer W_{ext} and W_s can be calculated. In particular, an x polarized incident electric field is assumed, so the scattered field thanks to equation 2.49 can be computed as:

$$E_s = \frac{e^{ik(r-z)}}{-ikr} X \; E_i \tag{2.54}$$

where X is the vector scattering amplitude that can be obtained thanks to equations 3.13 and 2.46:

$$X = (S_2 cos(\phi) + S_3 sin(\phi))\vec{e_{\|s}} + (S_4 cos(\phi) - S_1 sin(\phi))\vec{e_{\perp s}} \tag{2.55}$$

In general, rather then using the energy transfer W, surface-specific quantities, e.g. cross sectional areas (m^2) are introduced. These quantities represent the ratio between the energy transfer and the incident radiation:

$$C_{ext} = \frac{W_{ext}}{I_i} = \frac{4\pi}{k^2} Re(X \cdot \vec{e_x})_{\theta=0} \tag{2.56}$$

$$C_s = \frac{W_s}{I_i} = \int_0^{2\pi} \int_0^{\pi} \frac{|X|^2}{k^2} d\Omega \tag{2.57}$$

$$C_a = \frac{W_a}{I_i} = C_{ext} - C_s \tag{2.58}$$

2.4 Thermal Radiation

2.4.1 Fundamentals

The main three mechanisms to transfer thermal energy are conduction, convection and radiation. Conduction is associated to heat transfer due to collisions between molecules for solid and liquid, and to free electrons interactions in solid. The process that guides convection is very similar to conduction, but new molecules with lower kinetic energy are continuously provided to enhance the heat transfer mechanism (advection). The equations that govern these two process are in general linearly proportional to the temperature difference between the two systems involved in the heat transfer. The first is described by the Fourier's law:

$$q = -k\nabla T \tag{2.59}$$

where q is the specific heat in (W/m^2), k the thermal conductivity in (W/mK) and ∇T is the temperature gradient measured in K/m. The second mechanism is described by correlation in the form of:

$$q = h(T - T_\infty) \tag{2.60}$$

where h is the convective heat transfer coefficient measured in $W/(m^2K)$, T_∞ the temperature of the oncoming fluid and T the temperature of the body.
The third mode of heat transfer, namely radiation, is very different from the other two. In this case, heat is conveyed through electromagnetic waves. More specifically, thermal radiation is defined by the electromagnetic waves whose wavelength ranges from $0.1\mu m$ to $100\mu m$, meaning that it includes part of the ultraviolet till the mid infrared region (Figure 2.5).

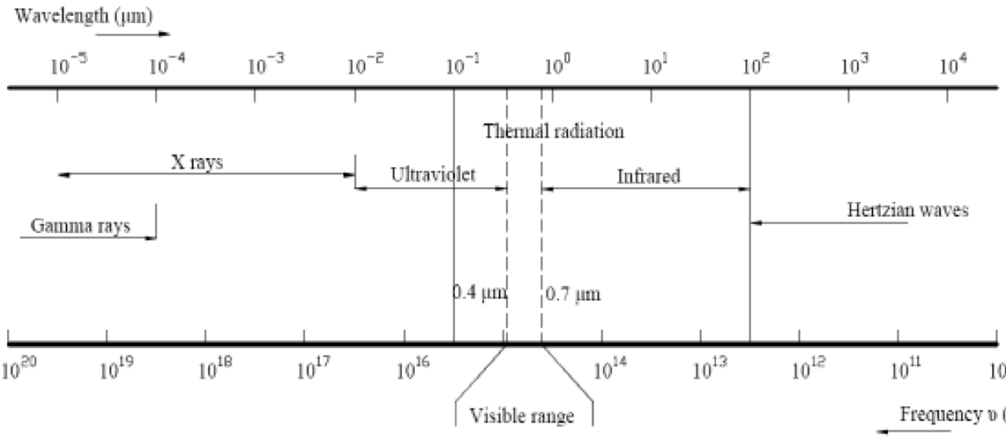

FIGURE 2.5: Electromagnetic spectrum (Figure from [12]).

The part of the electromagnetic spectrum approximately between 0.4 and $0.7\mu m$ embeds the *visible light*. The largest portion of thermal radiation includes the *infrared region*, which can be further subdivided in:

- Near infrared→ $0.7 - 1.4\mu m$
- Short wavelength infrared → $1.4 - 3\mu m$
- Mid wavelength infrared → $3 - 8\mu m$
- Long wavelength infrared → $8 - 15\mu m$

- Far infrared → $15 - 1000\mu m$

In addition, this third mode of heat transfer differs from the other two since it does not require a medium to propagates and, moreover, it is proportional to the fourth power of temperatures:

$$q \propto T^4 - T_\infty^4 \tag{2.61}$$

An other concept to introduce when analysing the thermal radiation is the "directionality". In particular, by considering an emitting surface dA, this emits radiation in all the directions since its temperature is different than $0K$. To account for the radiation only in one direction, the azimutal angle β and polar angle θ must be introduced, so that the direction $\vec{\gamma}$ is fully defined (Figure 2.6)

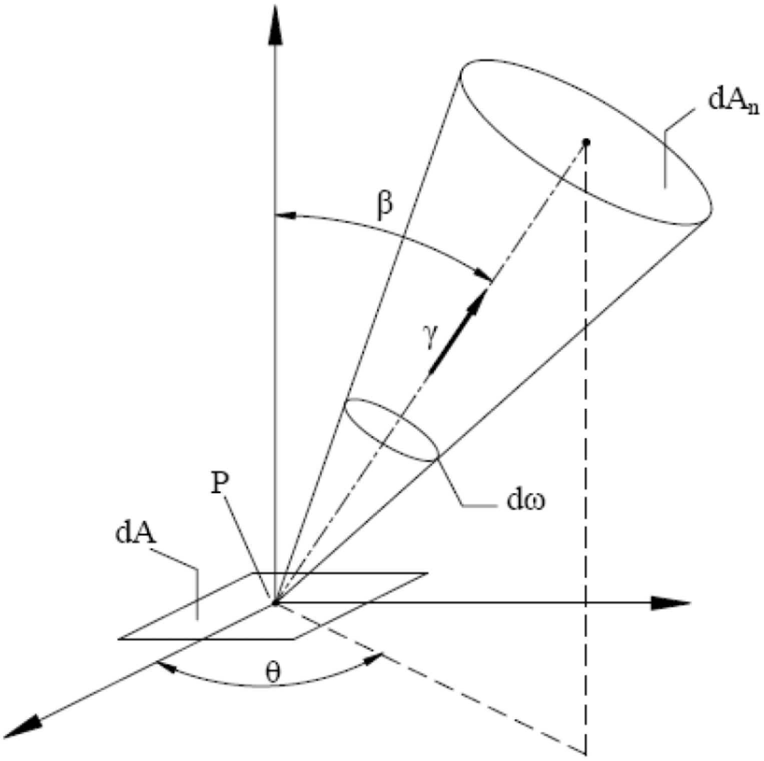

FIGURE 2.6: Description of the direction $\vec{\gamma}$ through the polar angle θ and the azimutal angle β; d represents the solid angle which is defined as $\frac{dA_n}{r^2}$ (Figure from [12]).

Thanks to this, the total radiative heat flux Φ is used to compute the following specific property:

$$i_{\lambda,\gamma} = \frac{\partial^3 \Phi}{\partial A cos(\beta) \partial\omega\partial\lambda} \tag{2.62}$$

where $i_{\lambda,\gamma}$ represents the spectral intensity which accounts for the fact that the behaviour of the emitting surface depends both on the wavelength λ and the direction ω. Thus, it is defined as the heat flux emitted per unit of surface per unit wavelength per unit solid angle in a specific direction.

To consider the radiation emitted in all the wavelength, equation 2.62 can be integrated for all the thermal spectrum obtaining the total intensity I_λ:

$$I_\lambda = \int i_{\lambda,\gamma} d\lambda \tag{2.63}$$

which represents the heat flux emitted per unit of surface per unit of solid angle in a specific direction:

$$I_\lambda = \frac{\partial^2 \Phi}{\partial A cos(\beta) \partial \omega} \tag{2.64}$$

Instead, to account for all the directions, equation 2.62 can be integrated over a whole semi sphere to obtain the hemispherical spectral emissive power:

$$e_\lambda = \int i_{\lambda,\gamma} cos(\beta) d\omega \tag{2.65}$$

which represents the heat flux emitted per unit area per unit wavelength considering all the directions:

$$e_\lambda = \frac{\partial^2 \Phi}{\partial A \partial \lambda} \tag{2.66}$$

Finally, by integrating equation 2.66 over all the wavelengths, the total emissive power E is computed as:

$$E = \int e_\lambda d\lambda = \int I_\lambda cos(\beta) d\omega = \frac{\partial \Phi}{\partial A} \tag{2.67}$$

In thermal radiation problems, a benchmark system that is generally introduced is the so called "blackbody". The latter consists in an ideal body that absorbs all the incident radiation without reflection or transmission. When considering the emission, the black body is a Lambert emitter, namely the emitted radiation does not depend on the direction. The emispherical spectral emissive power for a black body can be computed through Planck's law [12]:

$$e_\lambda = \frac{2\pi h c^2}{\lambda^5 \left(e^{\frac{hc}{k_b \lambda T}} - 1 \right)} \tag{2.68}$$

where c is the speed of the light, k_b the Boltzmann's constant and h the Planck's constant. Thus, for a black body, the spectrum is unique at a given temperature (Figure 2.7). In this case, equation 2.67 can be developed exploiting the diffuse emitter property of the black body and the Planck's law for the spectral emission, thus integrating over a semi-sphere:

$$E_b = \int I_\lambda cos(\beta) d\omega = \int_0^{2\pi} \int_0^{\pi/2} I_\lambda cos(\beta) sin(\beta) d\beta d\theta = \tag{2.69}$$

$$= 2\pi I_\lambda \int_0^{\pi/2} cos(\beta) sin(\beta) d\beta = \pi I_b \tag{2.70}$$

and exploiting equation 2.68:

$$E_b = \sigma T^4 \tag{2.71}$$

where σ is the Stephan-Boltzmann constant, thus pointing out that for a black body the emissive power is only function of the temperature.

More generally, the quantity "*emissivity*" is introduced for real bodies. The latter is defined as:

$$\epsilon = \frac{E}{E_b}, \tag{2.72}$$

where E is the emission of the real body and E_b the one of the corresponding black body at the same temperature. In general, the emissivity depends not only on the temperature, but also on the wavelength and the direction of propagation.

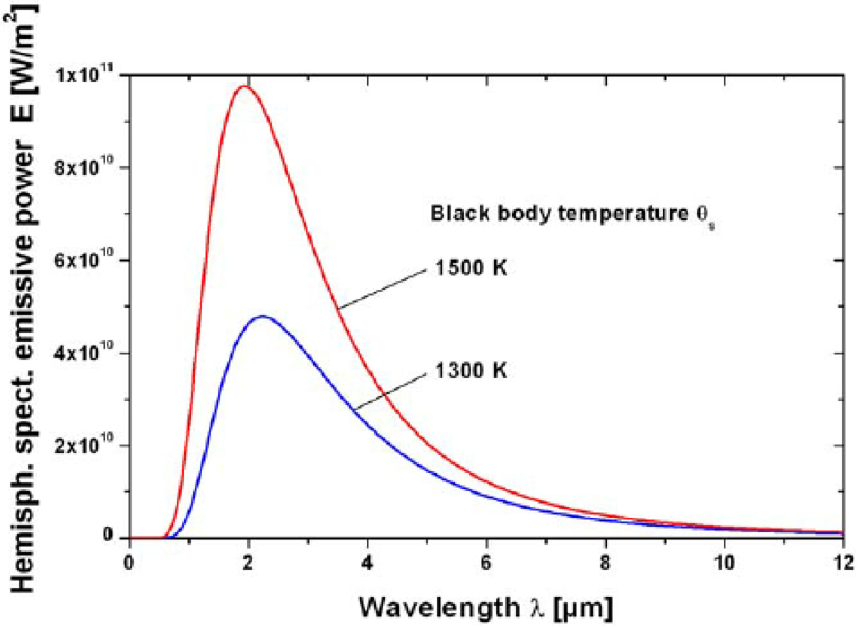

FIGURE 2.7: Hemispherical spectral emissive power of a black body for different temperatures (Figure from [13]).

2.4.2 Radiative Cooling

As described in section 1.4, one of the most important process that allows polyethylene fabrics to be a possible breakthrough innovation for the cooling industry is the so called "radiative cooling". The latter, whose mathematical framework is the one depicted in the previous paragraphs, is defined as the mechanisms through which a system cools down thanks to radiative heat transfer with an other system, e.g. the environment. Most importantly, this cooling mechanism differs from the other three (ACG, LCG, PCG) since it is completely passive, meaning that the cooling process occurs naturally without the need of an external energy source.

When analysing radiative cooling in the open ambient, the main contributions in the energy balance of the system under investigation are [14] (Figure 2.8):

1. Radiative heat emitted from the system at temperature $T_s \rightarrow q_{rad}(T_s)$
2. Conductive and convective heat losses $\rightarrow q_{loss}$
3. Heat absorbed from the sun$\rightarrow q_{solar}$
4. Heat exchanged with the atmosphere $\rightarrow q_{atm}$

where the net cooling power (W) of the system $q_{net,cooling}$ can be computed as:

$$q_{net,cooling} = q_{rad}(T_s) - q_{loss} - q_{solar} - q_{atm} \tag{2.73}$$

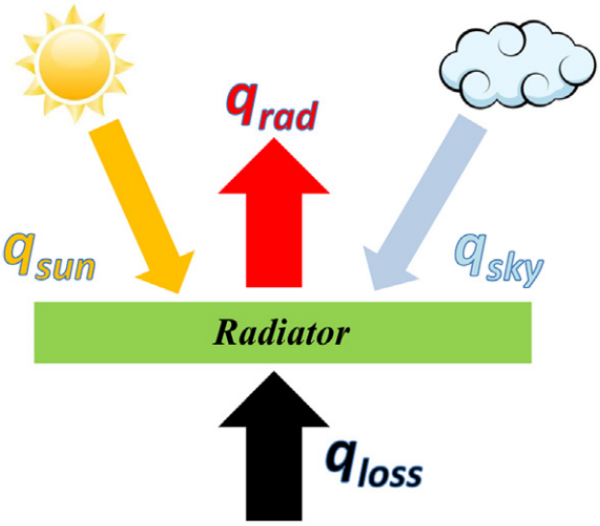

FIGURE 2.8: Thermal balance for a system that shows radiative cooling (Figure from [14])

1. Radiative heat

The radiative heat emitted by the system can be computed thanks to equation 2.67 and considering the definition of emissivity in equation 2.72

$$q_{rad}(T_s) = A_s \int_0^{\infty} \int_0^{2\pi} \int_0^{\pi/2} \epsilon_s I_b cos(\beta) sin(\beta) d\beta d\theta d\lambda \tag{2.74}$$

Specifically, when considering personal thermal management application, the system under investigation is the human body, thus further information about the emission from the skin are necessary.

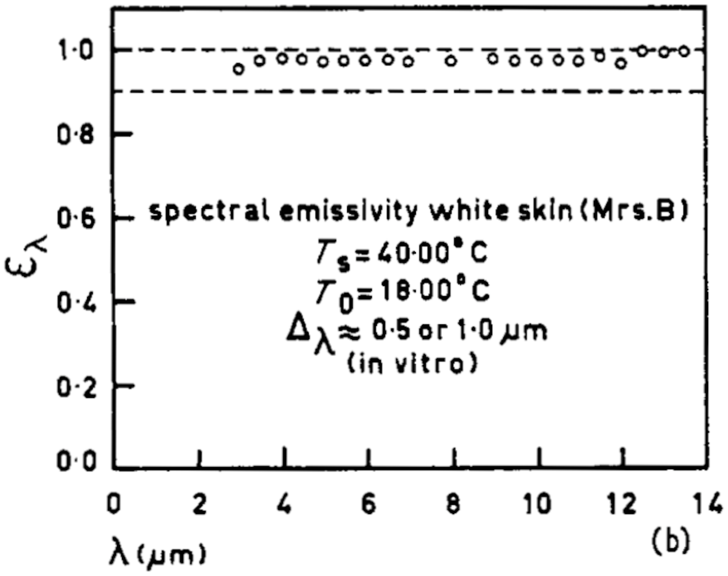

FIGURE 2.9: Experimental emission spectrum of white skin (Figure from [15]).

The first studies concerning this topic were performed in the early XXth century by Hardy [16] for medical applications, and further experiments have been conducted on real samples of skins in 1973 by Sketekee [15]. The latter shows that the emissivity of the skin is nearly unitary in the interval between 3 and 14 μm, thus the human body can be considered as a black body emitting between the mid (MWIR) and the large wavelength infrared (LWIR) (Figure 2.9). More recent and accurate analyses show that the emissivity is constant between 3 and 14 μm [17], specifically the body can be considered as a black body at a wavelength of 10.6μm [18].

2. Conductive and convective heat losses

Other than radiation, other sources of heat losses are conduction and convection. In the simplest case, the losses can be accounted thanks to equation 2.60:

$$q_{loss} = hA_s(T_s - T_{env}) \tag{2.75}$$

where T_{env} is the temperature of the environment and h is an heat transfer coefficient that encompasses both conduction and convection [19]. If $T_{env} < T_s$ then the losses would be negative, providing a positive effect on the cooling process of equation 2.73; on the contrary, in sub-ambient radiative cooling applications where the temperature of the environment is higher than the one of the system $T_{env} > T_s$, the overall losses generate a negative effect on the temperature of the system that would be increased.

3. Sun

The absorbed heat from the sun can be computed with the following expression [19]:

$$q_{sun} = A_s \int_0^{\infty} \epsilon(\lambda, \theta_{sun}) I_{AM,1.5}(\lambda) d\lambda \tag{2.76}$$

where θ_{sun} is the angle at which the system is facing the sun and $I_{AM,1.5}$ is the irradiance of the sun (Figure 2.10), which shows a peak in the visible region.

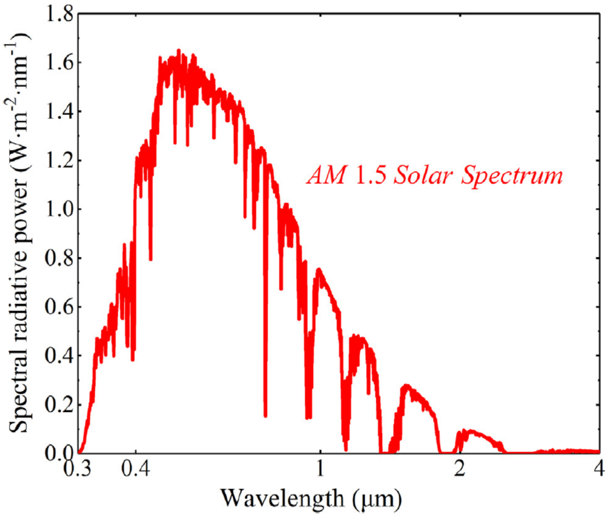

FIGURE 2.10: Spectral radiative power of the sun with an air mass coefficient AM of 1.5 (Figure from [14]).

For many applications the air mass coefficient, which is defined as:

$$AM = \frac{1}{cos(\theta_{sun})}, \tag{2.77}$$

is considered to be equal to 1.5, meaning that the zenith angle is θ_{sun} is 48.2^o. In this case the irradiance is 1000 W/m^2, slightly lower than solar illuminance beyond the atmosphere, which is 1357 W/m^2 [20].

4. Atmosphere

The atmosphere is composed mainly of nitrogen, oxygen and it behaves as a semi transparent radiative source in the infrared region. Thus, the heat absorbed by the system due to the radiation emitted from the atmosphere can be computed as [14]:

$$q_{atm} = A_s \pi \int_0^{\infty} \int_0^{\pi/2} \alpha_s I_{atm} sin(\beta) d\beta d\lambda \tag{2.78}$$

where I_{atm} is the radiative intensity of the sky and α_s the absorptivity of the system. One of the key element that allows to have radiative cooling for human body is the so called "atmospheric window" (Figure 2.11).

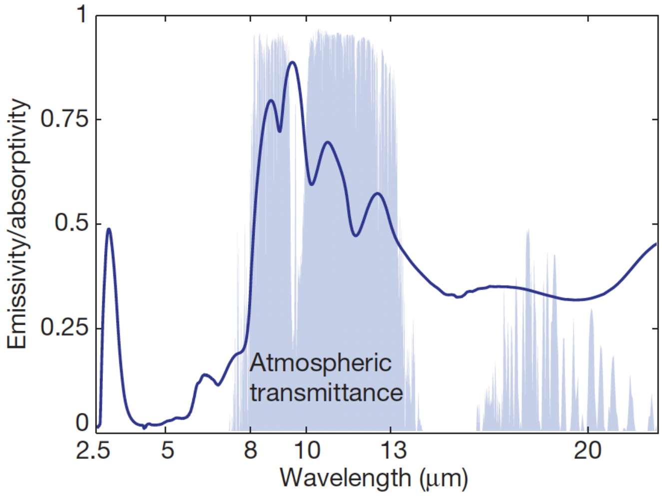

FIGURE 2.11: The continuous line describes a model for the transmission of the atmosphere in the infrared region which shows the so called "atmospheric window" between $8-13\mu m$, the spectrum instead shows measured data for a cooler that emits in the atmospheric window to fully exploit the radiative cooling effect (Figure from [19]).

In general, the atmosphere limits the radiative transfer between an object on the earth and the universe since it is a participating media that partially absorbs the emitted radiation. Despite this, in the range between $8-13\mu m$ it is highly transparent to the radiation. Thus, the heat exchange between the human body, which can be considered as a black body at $10.6\mu m$, and the universe is enhanced.

2.4.3 Absorption Spectra of Common Textiles

Based on the previous considerations, an ideal fabric for personal cooling applications should be:

- highly reflective in the visible range, so that it does not absorb the radiation from the sun and it is opaque to the human eye,
- highly transparent in the infrared region, so that it can transmit the heat emitted from the human body.

Specifically, if considering the radiation coefficients the ideal garment would show the characteristics reported in Table *1*.

Table 1. Radiative properties of an ideal fabric for daytime radiative cooling

	AM 1.5	LWIR-MWIR
A	0	0
T	0	1
R	1	0

Unfortunately, the common materials used in the textiles industry, e.g. cotton, show very different properties, , as shown in Table 2.

Table 2. Radiative properties of common fabric used in textile industry: cotton

	AM 1.5	LWIR-MWIR
A	0.1	1
T	0.5	0
R	0.4	0

This explains the poor thermal comfort that these garments provide during summer periods, where the ambient temperature is high. The high absorptivity in the infrared region causes the fabric to heat up and then to re-irradiate radiation to the body, which causes sweat and low comfort. A similar effect is caused by the low reflectance and higher transmittance in the visible region, which allows the radiation from the sun to easily reach the human body and increase its temperature.

These characteristics are due to the molecular structure of the different fabrics. As reported in [7], the most common garments such as cotton or polyester, which nowadays is very used for athletic fabrics, have a complicated molecular structure (Figure 2.12, 2.14) that translates in an higher number of absorption peaks, e.g. in the infrared region (Figure 2.13, 2.15).

Cotton is a fiber mostly made of cellulose, which is a natural compound made of glucose molecules (Figure 2.12).

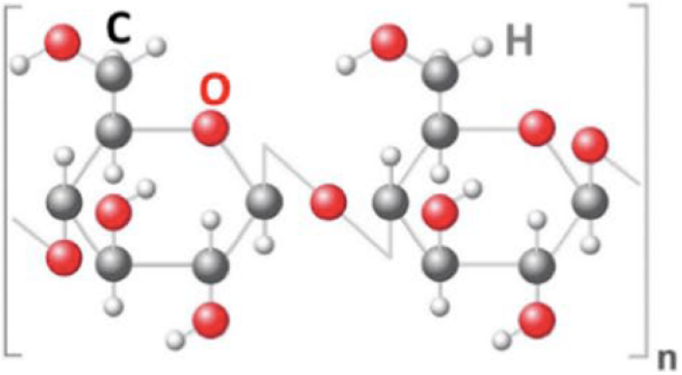

FIGURE 2.12: Molecular structure of cotton (Figure from [7]).

This complicated molecular structure reflects into an high absorptance in the MLIR and LWIR (Figure 2.13), which does not allow the heat emitted from the body to be transmitted into the environment.

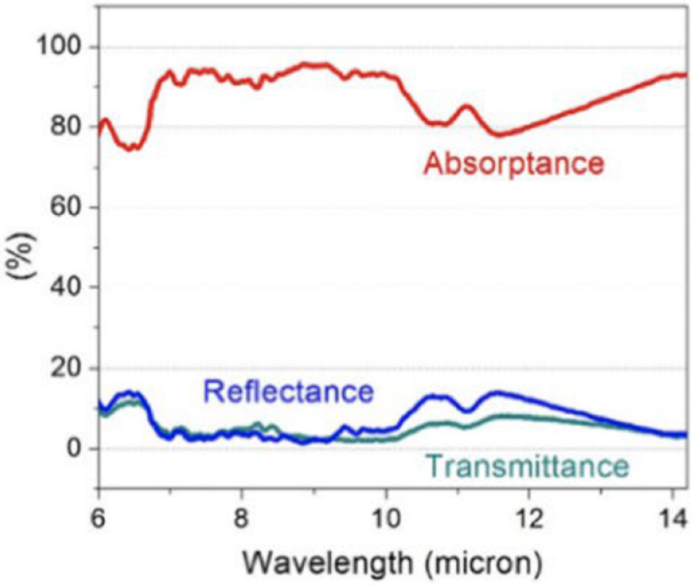

FIGURE 2.13: Infrared spectrum of cotton (Figure from [7]).

Similar results are obtained with polyester. The latter is a polymer that along its carbon chain presents ester functional groups (Figure 2.14).

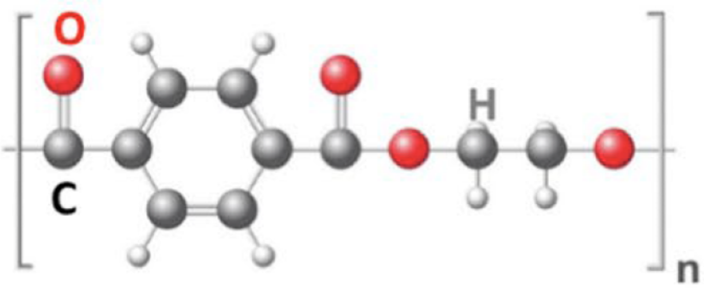

FIGURE 2.14: Molecular structure of polyester (Figure from [7]).

Also in this case the absorptance is very high in the infrared region, in addition the transmittance results to be even lower than the one of cotton (Figure 2.15), thus lower performances in terms of radiative cooling are expected with pure polyester.

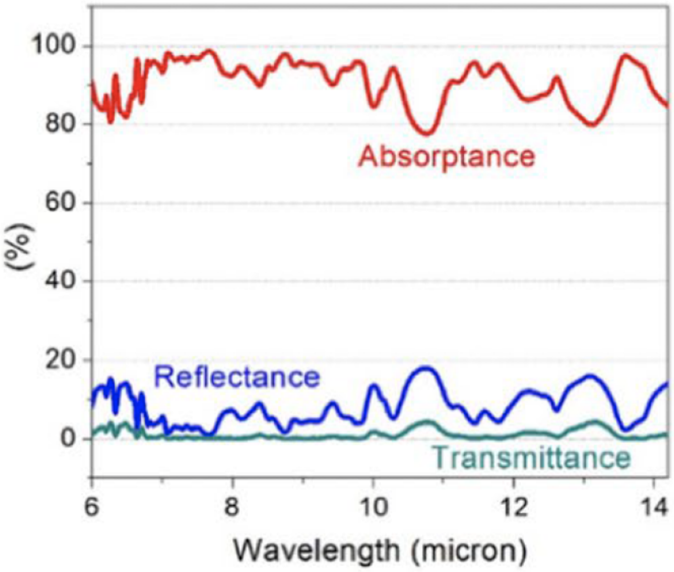

FIGURE 2.15: Infrared spectrum of polyester (Figure from [7]).

On the contrary, polyethylene has a simpler molecular structure formed just of carbon-oxygen bonds (Figure 2.16).

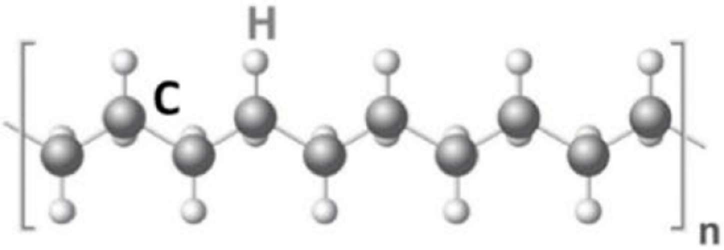

FIGURE 2.16: Molecular structure of polyethylene (Figure from [7]).

As demonstrated by [6], polyethylene presents fewer absorption peaks in the infrared region (Figure 2.17), thus having very similar characteristics to the one of an ideal fabric for radiative cooling.

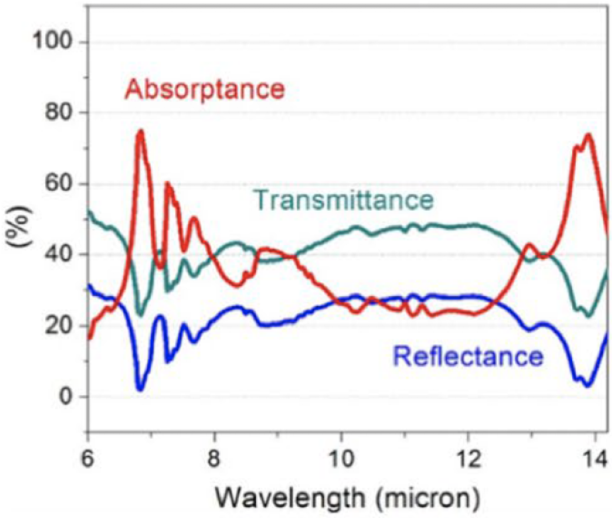

FIGURE 2.17: Infrared spectrum of polyethylene (Figure from [7]).

2.4.4 Experimental characterisation

The different absorption properties that the materials shows, reflect in different thermal performances. Thus, when they are used as human body garments, they allow to achieve different human skin temperature according on how much they reflect solar energy and transmit the infrared one. This section present the experimental set up that has been used to simulate the performance of the different garments (Figure 2.18).

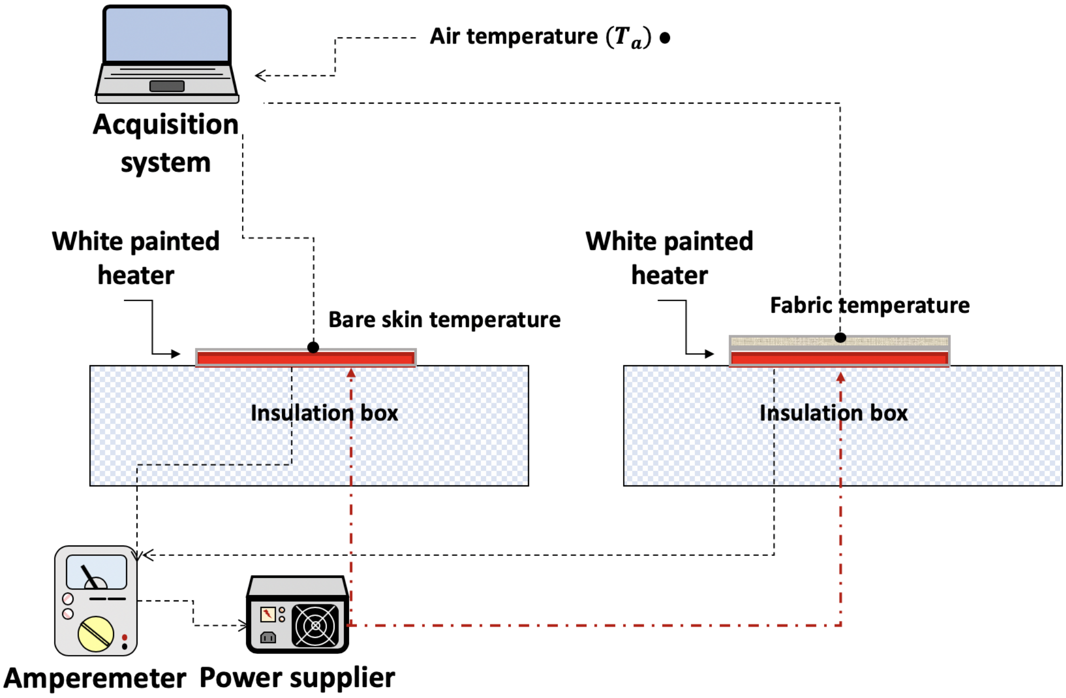

FIGURE 2.18: Experimental set up to assess the thermal performances of different garments.

Two specular set ups are built to record both the performances of the bare skin and the one of the skin covered with the garment. The human skin is simulated with a white painted heater that can provide a variable thermal load, similar to the one generated by the human metabolism. The skin is placed onto an insulation box (EPS, expanded polystyrene) to avoid thermal losses with the support, so that only the thermal performances due to different radiation properties of the fabrics can be evaluated. The temperatures of the system have been measured with three thermistors (Omega, Series 44000, depicted with a black dot in Figure 2.18):

- T1 to measure the temperature of the environment (open air or lab, depending if the experiment is performed outdoor or indoor, repsectively)
- T2 to measure the temperature of the bare skin in the centre of the heater
- T3 to measure the temperature of the skin under the fabrics in the centre of the heater

The power is supplied to the heaters thanks to a power supplier controlling the input voltage: the heaters have been connected in parallel to assure the same power to both of them. An amperometer has been connected to compute the current circulating in the circuit in series with the power supplier. Thus, the power (W) generated by the single heater can be computed as:

$$P = \frac{VI}{2}, \tag{2.79}$$

where V is the voltage imposed by the power supplier and I is the current read with the amperometer at the end of the circuit, which is supposed to be equally split in the two heaters (which have the same electrical resistance).

The experiments have been performed both in indoor and outdoor conditions, and the common protocol that has been followed for each type of fabric is:

1. Switch on the two heaters (without any garment yet) and wait for the stationary temperatures
2. Once reached the steady state, place the fabric upon one of the two heaters and wait for the achieving the steady state again
3. Finally compute the difference between the stationary temperatures:

   $$\Delta T = T_{covered} - T_{skin}, \tag{2.80}$$

   where $T_{covered}$ is the stationary temperature of the skin covered with the fabric and T_{skin} is the stationary temperature of the bare skin.

This procedure has been applied to different types of garments and materials. For radiative cooling applications, the lower the ΔT between the skin covered with the fabric and the bare skin, the better it is. In fact, in that case, the garment allows to transmit a much higher portion of the heat emitted by the radiator, thus enabling a better thermal comfort for the human body.

Chapter 3

Transport in Porous Medium

This chapter addresses the second phenomenon involved in personal thermal management application, namely transport in porous medium. The latter is responsible for the spread of sweat through the fabric: in general, a wider and faster spread allows a faster evaporation of the sweat, which guarantees a better comfort for the human body.

The topic of water transport in porous medium is very wide: in this section the mathematical formulation for an isothermal single phase flow is presented, then a insight about the experimental procedures to characterise the main transport parameters is proposed.

3.1 Physical background

Considering a porous medium, the porosity ϕ is defined as the fraction between the volume of the pores and the total volume of the medium:

$$\phi = \frac{V_{pores}}{V_{tot}} \tag{3.1}$$

In general, a formulation based on continuum approach is used also for porous medium, thus a representative element volume (RVE) is introduced [21]. The size of the RVE is bigger than that of the pores, so that averaged quantities, e.g. velocity, are robust and not affected by the RVE size. When shifting towards a continuum formulation, the quantities of interest can be averaged in two ways:

- over the total volume of the medium V_{tot}, thus encompassing both the fluid and the solid
- over the volume of the fluid V_f

For example, considering the velocity of the fluid, the average fluid speed over the total volume V_{tot} is denoted as v and is called *Darcy velocity*. On the contrary, the average fluid speed over the volume of the fluid is denoted as V and called *intrinsic average velocity*. The relation between the two is expressed by the Dupuit–Forchheimer relationship [21] :

$$v = \phi V. \tag{3.2}$$

3.1.1 Continuity Equation

After introducing a continuum model, the classical conservation law for the fluid mass can be expressed:

$$\phi \frac{\partial \rho_f}{\partial t} + \nabla \cdot (\rho_f v) = 0 \tag{3.3}$$

where ρ_f is the density of the fluid, ϕ the porosity of the medium and v the Darcy velocity. Specifically, for the case of transport in fabric, a further consideration about the porosity is necessary. The structure of the garment, which consists of multi filament yarns woven into textiles, allows the water to spread only within the yarn, while the space between different yarns remains saturated of air (Figure 3.1).

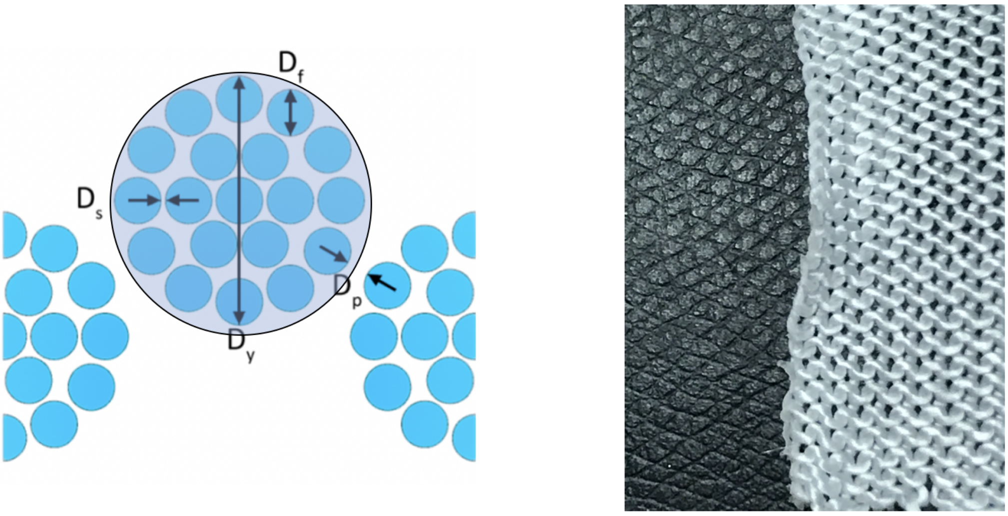

FIGURE 3.1: The fabric is composed of different yarns (black circle) woven one with the other to form the textiles. The yarn itself is composed of multiple fibers of diameter D_f, the water can spread only within the yarn, thus the space between different yarns remain saturated of air. In fact, if observing the picture on the right, the fabric is completely wet, but the space within the yarn is saturated of air and the black background can be easily seen.

For this reason the "effective wicking porosity" must be introduced. The latter considers that water can spread only between the single fibers D_f separated one from the other by the average minimum distance D_s. On the contrary the space D_p, namely the space between different yarns, is saturated of air. Thus, the wicking effective porosity can be expressed as:

$$\phi_e = \phi(1 - S_{irr,air}) \tag{3.4}$$

where $S_{irr,air}$ is the irriducible fraction of air defined as:

$$S_{irr,air} = \frac{V_{nw,pores}}{V_{pores}} \tag{3.5}$$

and $V_{nw,pores}$ represents the not wetted volume of the pores between the yarns. For this reason, equation 3.3 for the specific case of fabric can be re-written as:

$$\phi_e \frac{\partial \rho_f}{\partial t} + \nabla \cdot (\rho_f v) = 0 \tag{3.6}$$

3.1.2 Momentum Equation

In continuum mechanics, the momentum equation is often expressed in term of the Navier - Stokes equation, here an analogue formulation for porous medium is proposed [21]. The first experimental studies concerning this topic have been performed by Henry Darcy at the beginning of the XIX century, where he found out that the speed of the fluid is directly proportional to the pressure difference. In the case of unidirectional flow, the relation becomes:

$$v = -\frac{K}{\mu}\frac{\partial P}{\partial x} \tag{3.7}$$

where v is the Darcy velocity (m/s), K is the specific permeability (m^2) which is an intrinsic property of the medium and does not depend on the type of wicking fluid, μ is the dynamic viscosity of the fluid (m^2/s) and $\partial p/\partial x$ is the pressure gradient (Pa/m) along the direction of motion x.
More generally, for an anisotropic material the Darcy relation can be expressed in matrix form as:

$$\begin{bmatrix} v_x \\ v_y \\ v_z \end{bmatrix} = -\frac{1}{\mu} \begin{bmatrix} K_x & 0 & 0 \\ 0 & K_y & 0 \\ 0 & 0 & K_z \end{bmatrix} \begin{bmatrix} \partial P/\partial x \\ \partial P/\partial y \\ \partial P/\partial z \end{bmatrix} \tag{3.8}$$

Based on Darcy's studies, other researchers retrieved a formulation of the momentum equation for porous medium by analogy with the Navier Stokes' equation. For example, in 1957 Wooding [21] developed equation 3.7 by considering also gravity and inertial effects:

$$\rho_f \left[\frac{\partial V}{\partial t} + (V \cdot \nabla) V \right] = -\nabla P - \frac{\mu}{K} v, \tag{3.9}$$

which represents a specular formulation of Navier Stokes' equation with an additional momentum sink represented by the Darcy term $-\frac{\mu}{K}v$, due to the resistance that the porous medium exerts on the wicking fluid.

In textile applications, it is very common to express the position of the water front in the porous medium as a function of time. If considering equation 3.3 under the incompressible limit assumption, the latter becomes:

$$\nabla \cdot v = 0 \tag{3.10}$$

Then, by substituting the Darcy relation 3.7 in equation 3.10:

$$-\frac{K}{\mu}\frac{\partial^2 P}{\partial x^2} = 0, \tag{3.11}$$

which can be simplified as:

$$\frac{\partial^2 P}{\partial x^2} = 0. \tag{3.12}$$

The latter is a ordinary differential equation whose solution is in the form:

$$P(x) = c_1 x + c_2, \tag{3.13}$$

being c_1 and c_2 two constants that can be identified by imposing two boundary conditions.
P, as explained in section 3.1, represents the intrinsic average pressure, in particular:

$$P = p + \rho g h, \tag{3.14}$$

where p is the hydrodynamic pressure and h the height of the fully saturated water front (sharp front approximation).
When considering a vertical imbibition process (along x direction), the two boundary conditions can be formulated as:

$$P = p_{atm} \qquad at\ x = 0 \tag{3.15}$$

$$P = p_{atm} + \rho g h_f - p_c \qquad at\ x = h_f \tag{3.16}$$

The first boundary condition represents the entry averaged pressure of the liquid into the fabric; the second is the averaged pressure at a general front at height h_f (function of time) which is a mechanical balance between the atmospheric pressure p_{atm}, the pressure due to the column of liquid $\rho g h_f$ and the capillary pressure p_c which drives the wicking adsorption in the capillary.
By imposing the equations 3.15 and 3.16 in the expression for the pressure in equation 3.13, the two constants can be computed:

$$c_2 = p_{atm} \tag{3.17}$$

$$c_1 = \rho g - \frac{p_c}{h_f} \tag{3.18}$$

Thus equation 3.13 becomes:

$$P(x) = p_{atm} + \rho g x - \frac{p_c}{h_f} x, \tag{3.19}$$

which expresses the averaged pore pressure at a general liquid front position.
By considering the incremental change in the front position, namely dh_f/dt, to be equal to the intrinsic averaged velocity at the water front, the following relation holds [22]:

$$\frac{dh_f}{d_t} = -\frac{v}{\phi_e}. \tag{3.20}$$

By exploiting the Darcy relation 3.7, the right hand side can be re-written as:

$$-\frac{v}{\phi_e} = -\frac{K}{\phi_e \mu} \frac{dP}{dx}, \tag{3.21}$$

and when substituting equation 3.19 in the latter expression:

$$-\frac{v}{\phi_e} = -\frac{K}{\phi_e \mu} \left(\frac{p_c}{h_f} - \rho g \right). \tag{3.22}$$

Finally, equating equations 3.22 and 3.20:

$$\frac{dh_f}{d_t} = -\frac{K}{\phi_e \mu}\left(\frac{p_c}{h_f} - \rho g\right) \tag{3.23}$$

This expression is a ordinary differential equation in h_f ,which can be solved thanks to separation of variable technique and by imposing that $h_f(t = 0) = 0$. In this case the solution becomes:

$$p_c ln\left|\frac{p_c}{p_c - \rho g h_f}\right| - \rho g h_f = \frac{\rho^2 g^2 K}{\phi_e \mu} t \tag{3.24}$$

The latter is an implicit expression, thus to make it explicit the Lambert function W can be used [22]. This function in general is used to transform an expression of the type:

$$y = W(z)e^W(z) \tag{3.25}$$

into a second one of the type:

$$z = W(y). \tag{3.26}$$

Specifically, in this case it is possible to obtain that:

$$h_f = \frac{p_c}{\rho g}\left[1 + W\left(-e^{-1-\frac{\rho^2 g^2 K}{\phi_e \mu p_c} t}\right)\right] \tag{3.27}$$

that gives an expression for the liquid front position during time.
In the simpler case where the effect of gravity is neglected, equation 3.23 can be integrated obtaining:

$$h_f = \sqrt{\frac{2Kp_c}{\phi_e \mu}}\sqrt{t} \tag{3.28}$$

that is commonly known as Lucas-Washburn equation.

Concluding, equations 3.28 and 3.27 can be used to model the wicking of water within the fabric knowing the three main parameters that identify the properties of the medium:

- Wicking effective porosity ϕ_e;
- Capillary pressure p_c;
- Permeability K.

3.2 Experimental Characterisation

This section shows the experimental method that has been used to compute the three main parameters regulating the wicking process within the garment, namely the effective wicking porosity ϕ_e, capillary pressure p_c and intrinsic permeability K. After this, an overview about the uncertainty quantification of the experimental results is proposed.

3.2.1 Wicking Effective Porosity

The effective wicking porosity ϕ_e is computed thanks to the so called "mass method", under the assumption of sharp front approximation [23]. The latter implies that between the fully saturated zone, namely where the fabric is totally wet, and the fully dry zone, namely the zone that has still to be reached by the fluid, there is no transition zone of partial wetting.
Under this assumption, during a vertical imbibition test (Figure 3.2) the mass of water absorbed by the fabric m_f can be expressed by recalling the definition of density [23]:

$$m_f = \rho_f V_f = A h_f \phi_e \rho_f \tag{3.29}$$

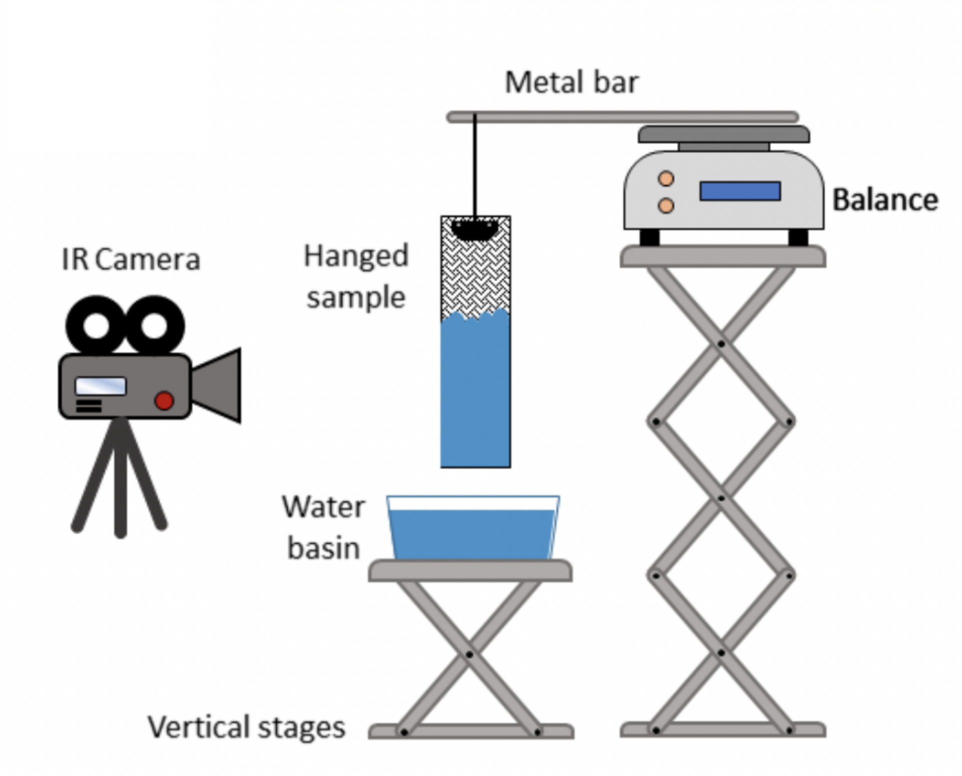

FIGURE 3.2: Experimental set up used to compute the effective wicking porosity ϕ_e

In particular, if considering an interval of time $\Delta t = t - t_0$, the latter equation can be re-written as:

$$m_{\Delta t} = \rho_f V_f = A h_{\Delta t} \phi_e \rho_f, \tag{3.30}$$

where V is the volume of the water within the porous medium, $A = \bar{s}\bar{w}$ is the cross section of the sample whose average thickness and width are $\bar{s}$ and $\bar{w}$ respectively, and $h_{\Delta t}$ the height reached by the liquid front after the time Δt. The width of the samples is measured with a calibre in five different positions, while their average thickness is evaluated by a micrometre superimposing the specimens, repeating the measurement in five random position on the sample, and dividing the average result by the number of specimens to reduce the relative error.

The set up aims to measure two main quantities that are usefull to compute the porosity:

- the imbibition mass $m_{\Delta t}$
- the height reached by the liquid front after a certain interval of time $h_{\Delta t}$

To measure the mass, a precision balance is placed on a vertical stage. A cantilever metal bar is fixed on top of the balance and used to hang the textile samples. A second vertical stage is used to support and move the distilled water. Six samples of the material under investigation are prepared and vertically dipped into distilled water for five and ten minutes, respectively. The procedure is repeated with three different samples of the same textile type, and the results averaged.

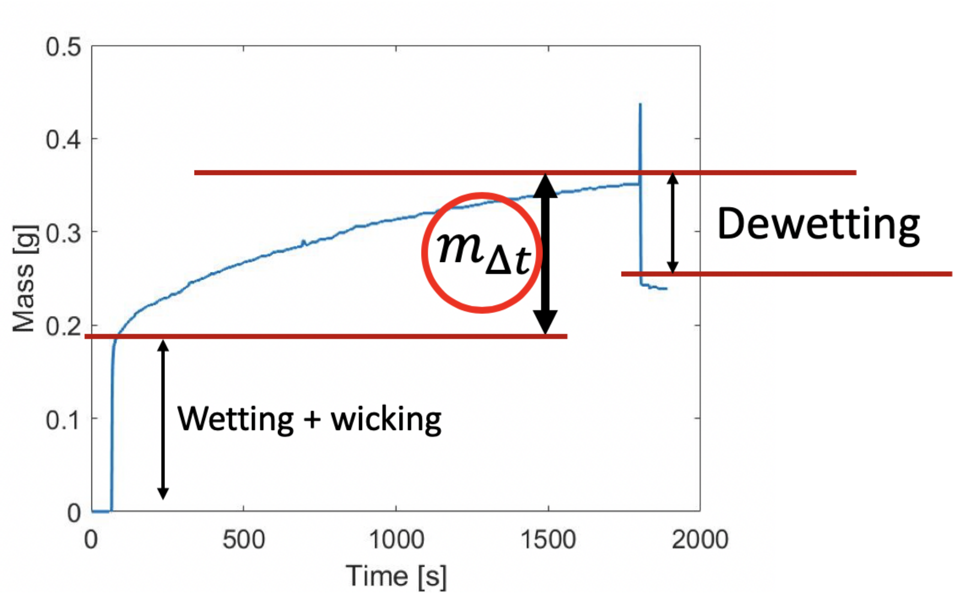

FIGURE 3.3: Profile of the imbibition mass in a vertical test ,which shows three different phases: wetting, wicking and dewetting

The transient behaviour of the imbibition mass shows three different phenomena (Figure 3.3):

1. Initial step due to the formation of the meniscus between the water basin and the fabric (wetting), and contemporary initial wicking
2. Wicking only absorption, here the mass is absorbed through the fabric by capillarity
3. Final step when the sample is extracted from the water basin (de-wetting process), and the meniscus is detached from the fabric.

The wicking mass $m_{\Delta t}$ that is present in the equation 3.30 is computed accounting just for the wicking process in step 2, thus the initial wicking in step 1 has been neglected.

For each sample, the height reached by the front $h_{\Delta t}$ is recorded with an infrared camera and then measured thanks to a support vector machine algorithm implemented in Matlab. (Figure 3.4).

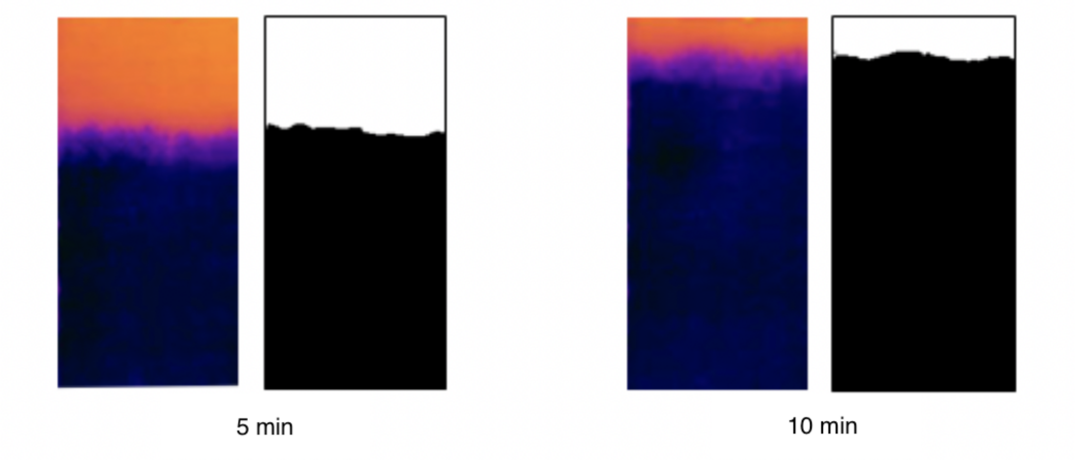

FIGURE 3.4: Frames of the infrared camera used to compute the imbibition height $h_{\Delta t}$ after 5 and 10 minutes. The left infrared image is converted in a black and white frame by using Matlab software in order to measure the height of the front.

By knowing the two quantities $m_{\Delta t}$, $h_{\Delta t}$ and using the expression 3.30, the wicking effective porosity can be computed from the slope of the curve (Figure 3.5):

$$Ah_{\Delta t} = \alpha m_{\Delta t} \tag{3.31}$$

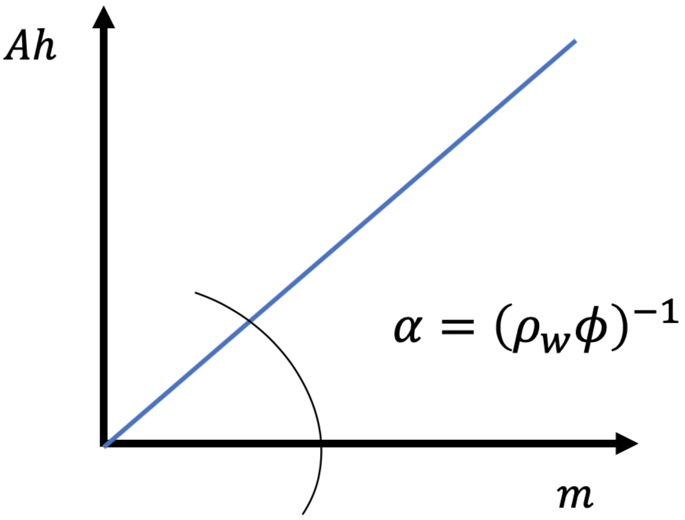

FIGURE 3.5: Plot of the imbibition height $h_{\Delta t}$ as a function of the imbibition mass $m_{\Delta t}$, the slope of the curve is fit on the experimental data and it is proportional to the effective wicking porosity ϕ_e.

where the parameter α is computed through least square fitting and is used to compute the porosity as:

$$\phi_e = \frac{1}{\alpha \rho_f} \tag{3.32}$$

3.2.2 Capillary Pressure

The experimental set up used to compute the capillary pressure p_c is the same used for the wicking porosity. In fact, based on Jurin's law, the capillary pressure can be computed as:

$$p_c = \rho_f g h_{max}, \tag{3.33}$$

where h_{max} is the maximum height reached in a vertical imbibition test (Figure 3.2). In this case, the scale is used only to check that the suction of water has reached a stationary state (Figure 3.6). at this instant the stationary imbibition mass is reached and the height is recorded with the infrared camera.

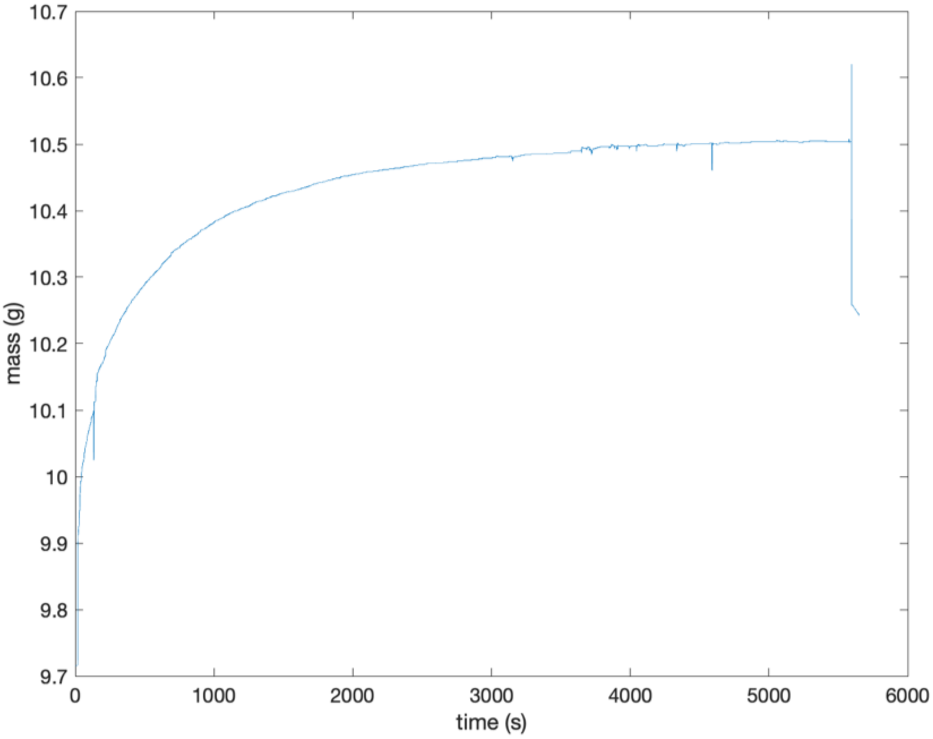

FIGURE 3.6: Transient profile of the imbibition mass used in a vertical imbibition test.

The imbibition mass is considered at steady state when the standard deviation of 1000 samples is lower than 10^{-3} g, considering a sampling frequency of 3 samples/s. The measure is repeated with three samples and results averaged.

3.2.3 Water Permeability

After computing the wicking effective porosity and the capillary pressure, the permeability can be fitted using the model of Lucas-Washburn (Figure 3.2).

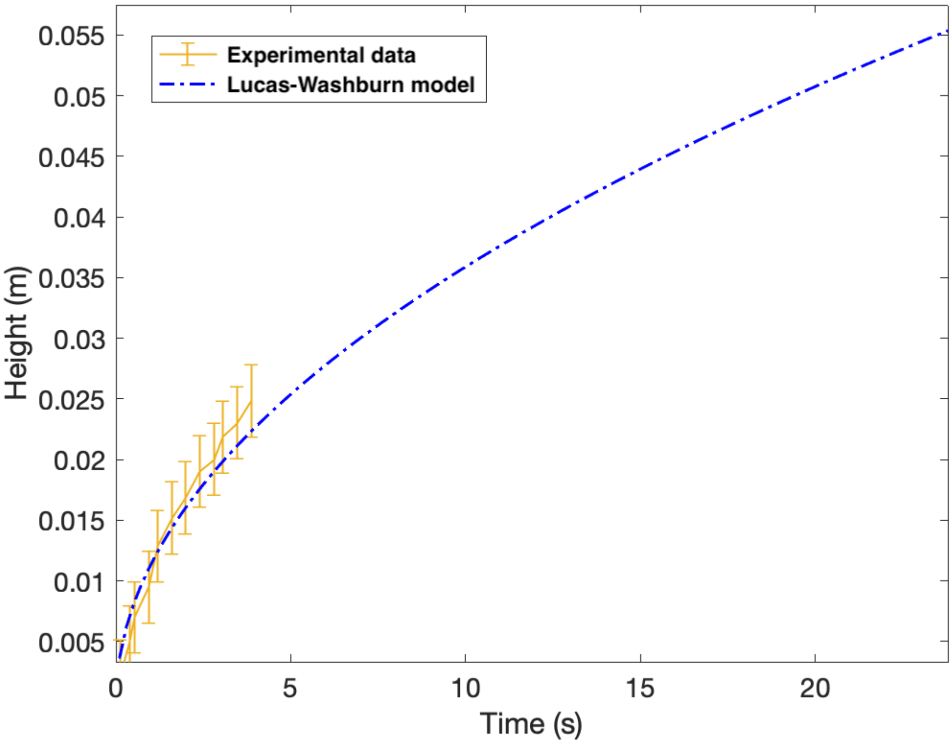

FIGURE 3.7: The Lucas-Washburn model is used to fit the horizontal experimental imbibition distances in order to extract the value of the permeability K. The error bars are computed based on equation 3.38.

In this case, the fitting parameter Θ is introduced:

$$h_{\Delta t} = \Theta\sqrt{t} \tag{3.34}$$

The least square method is applied to experimental data performed in a horizontal imbibition process (Figure 3.8), so that the effect of gravity is negligible and the Lucas Washburn model holds (Figure 3.7).

Finally, the permeability K (m^2) can be extracted from the fitting parameter Θ as:

$$K = \frac{\Theta\phi_e\mu}{2p_c}. \tag{3.35}$$

FIGURE 3.8: Horizontal imbibition test used to measure the wicking distances at a given time $h_{\Delta t}$.

The horizontal set up consists in a basin of distilled water where the left extremity of the fabric is immersed 1 *mm*; the fabrics lays on a hydrophobic support of Teflon, so that only the capillarity effect due to the fibers is considered. Moreover, the advancing front in time is recorded with an infrared camera, whose frames are then post processed with Matlab software to compute the imbibition distances $h_{\Delta t}$.

3.2.4 Uncertainty Quantification

The expanded uncertainty on the experimental measurements has been computed according to the NIST standard [24]:

$$U = k\sqrt{u_A^2 + u_B^2}, \tag{3.36}$$

where u_A expresses the uncertainty component estimated by statistical analysis of the measured values (type A), u_B refers to the uncertainty components evaluated by other means (type B), e.g. a priori information of the instruments such as calibration, accuracy and resolution, and k=2 is the coverage factor.

Uncertainty on the wicking distance

For what concerns the uncertainty on the measured position of the water front $h_{\Delta t,i}$, it is computed as:

$$u_{h_{\Delta t}} = \sqrt{\left(\frac{u_s}{2\sqrt{3}}\right)^2 + \left(\frac{u_{f,i}}{2\sqrt{6}}\right)^2}, \tag{3.37}$$

where u_s is the length of the fabric immersed in the water basin, which is of 1 *mm* for horizontal imbibition tests and of 2 *mm* for vertical tests both considered as uniformly distributed, $u_{f,i}$ is the thickness of the water front considered with a triangular distribution probability.

The expanded uncertainty is thus computed as:

$$U_{h_{\Delta t}} = k\sqrt{\frac{\sum_i^N u^2_{h_{\Delta t,i}}}{N^2} + \frac{R^2}{N}}, \tag{3.38}$$

where $R = \frac{max(h_{\Delta t,i}) - min(h_{\Delta t,i})}{2}$ is the statistical uncertainty within the repetitions N.

Uncertainty on the wicking effective porosity

The expanded uncertainty for the wicking porosity is computed based on the expression 3.31 and the fitting parameter α:

$$Ah_{\Delta t} = \alpha m_{\Delta t}.$$

Recalling that:

$$\phi_e = \frac{1}{\alpha \rho_f},$$

the contributions that affect the uncertainty come both from the uncertainty on the water front position $h_{\Delta t}$ (computed in the previous section) and the measurement of the thickness and width $\bar{s}$, $\bar{w}$ that are used to compute the area A. Introducing the quantity Y_i:

$$Y_i = Ah_{\Delta t,i}, \tag{3.39}$$

its standard uncertainty can be computed as:

$$u_{Y,i} = \sqrt{\left(\frac{\partial Y_i}{\partial h_{\Delta t,i}} u_{h_{\Delta t,i}}\right)^2 + \left(\frac{\partial Y_i}{\partial \bar{s}_i} u_{\bar{s}_i}\right)^2 + \left(\frac{\partial Y_i}{\partial \bar{w}_i} u_{\bar{w}_i}\right)^2}, \tag{3.40}$$

where the standard uncertainty $u_{\bar{s}_i}$ and $u_{\bar{w}_i}$ are computed as:

$$u_{\bar{G}_i} = \sqrt{\left(\frac{u_c}{2\sqrt{3}}\right)^2 + \left(\frac{max(G_{i,j}) - min(G_{i,j})}{2}\right)^2}, \tag{3.41}$$

being G either w or s, the index $j = (1;\ldots;5)$ the five repetitions of the measurement for the i-th sample, and $u_c = 10^{-3} m$ and $u_c = \frac{2.5}{3} 10^{-6} m$ the resolution of the measurement instrument for the width and thickness, respectively.
Finally, the fitting parameter α and its standard uncertainty s_α are used to computed the expanded uncertainty on the porosity as:

$$U_{\phi_e} = k\frac{2}{\rho_f \alpha^2} s_\alpha \tag{3.42}$$

Uncertainty on the permeability

The permeability is computed thanks to equation 3.34:

$$h_{\Delta t} = \Theta\sqrt{t}$$

thus its the standard uncertainty $u_{K,i}$ is:

$$u_{K,i} = \sqrt{\left(\frac{\partial K_i}{\partial \Theta} u_\Theta\right)^2 + \left(\frac{\partial K_i}{\partial p_c} u_{p_c}\right)^2 + \left(\frac{\partial K_i}{\partial \phi_e}, u_{\phi_e}\right)^2} \tag{3.43}$$

where u_Θ is the standard uncertainty on the fitting parameter as from the least square method, $u_{p_s} = \rho g u_{h_{max}}$ is the standard uncertainty on the capillary pressure evaluated from the standard uncertainty on the maximum height, and u_{ϕ_e} is the standard uncertainty on the wicking effective porosity, evaluated as described in the previous section. Finally, the related expanded uncertainty can be evaluated according to equation 3.38.

Chapter 4

Results

This chapter aims to present the main findings of the research, which specifically addresses the three topics presented in section *1.4*: **T1**, **T2** and **T3**

Different types of low density polyethylene textiles with different weaving parameters have been analysed (Figure), in particular:

- Woven PE: multiple yarns are woven perpendicularly one with the other to form the grain
- Knitted PE: a single yarn is looped to form the grain. Specifically two variants with different yarn thickness, namely Knitted 1 and Knitted 2, are tested.

In addition, other materials have been used as benchmarks to compare their properties with the ones of polyethylene fabrics:

- Dyneema: commercial material composed of ultra high molecular weight knitted polyethylene to which micro-particles are added in each fiber to increase its strength. Generally it is not used for personal fabrics since its very high rigidity makes it more suitable for other applications, e.g. ropes for constructions or cut resistant gloves.
- Polyester: largely adopted in textile industry for high performance clothes
- Cotton: one of the most common material for textiles

FIGURE 4.1: Polyethylene fabrics used in the characterisation: woven, knitted1, knitted2, Dyneema. The two knitted samples differs for the yarn thickness, which is 0.28 *mm* for the first and 0.43 *mm* for the second.

4.1 Structural Characterisation

The polyethylene fabrics have been produced by external industrial partners, i.e. AFFOA Advanced Functional Fabric of America, thus a structural characterisation is needed to measure the real diameters of the fibers and gain a better insight on the weaving technique.

This structural characterisation is performed with the Zeiss scanning electron microscope (SEM), model Merlin, shown in Figure 4.2. In this technique, the samples must be electrically conductive, thus they were coated with a 50 nm carbon layer to increase the conductivity of the material. The resolution of SEM is around 20 nm, meaning that you can not achieve enough resolution to distinguish atoms as it is possible with other techniques, e.g. transmission electron microscope (TEM).

FIGURE 4.2: Zeiss scanning electron microscope, model Merlin, used for the structural characterisation of textiles.

The frames that the SEM is able to capture allows to measure both the diameter of the fibers and the diameter of the yarns. Here, some examples for woven PE (Figure 4.3, 4.4) and Dyneema (Figure 4.5, 4.6) are reported.

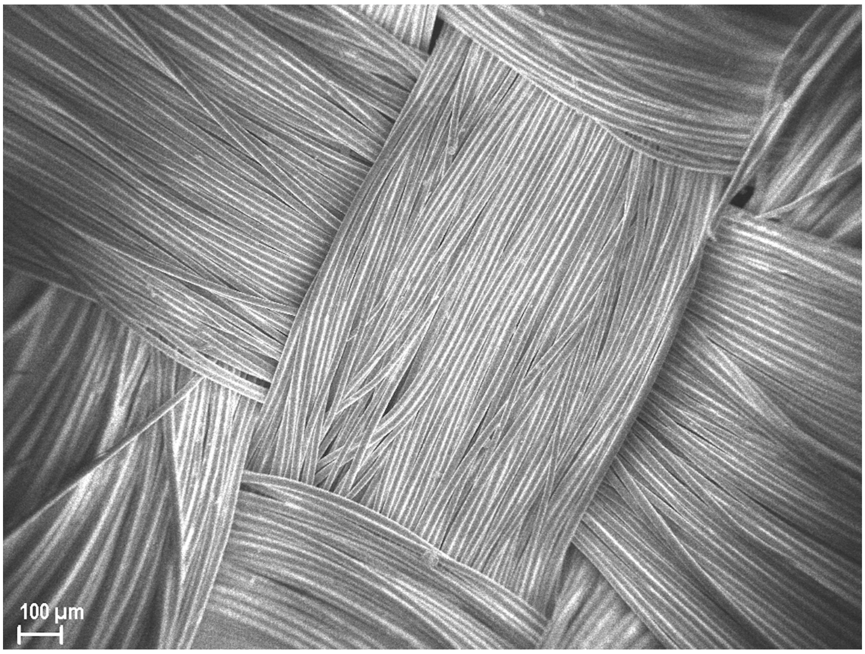

FIGURE 4.3: SEM image of the woven PE, which shows the yarn structure typical of woven textiles. The yarn diameter is about 800 μm.

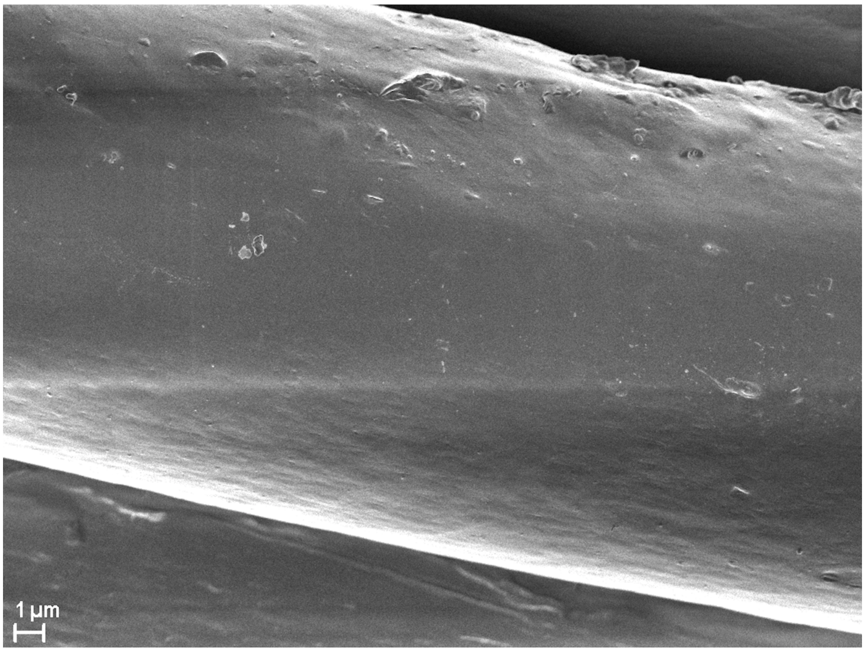

FIGURE 4.4: SEM image of the woven PE, which shows fiber diameter about 25 μm.

FIGURE 4.5: SEM image of the Dyneema, which shows the yarn structure typical of knitted textiles. The yarn diameter is about 600 μm.

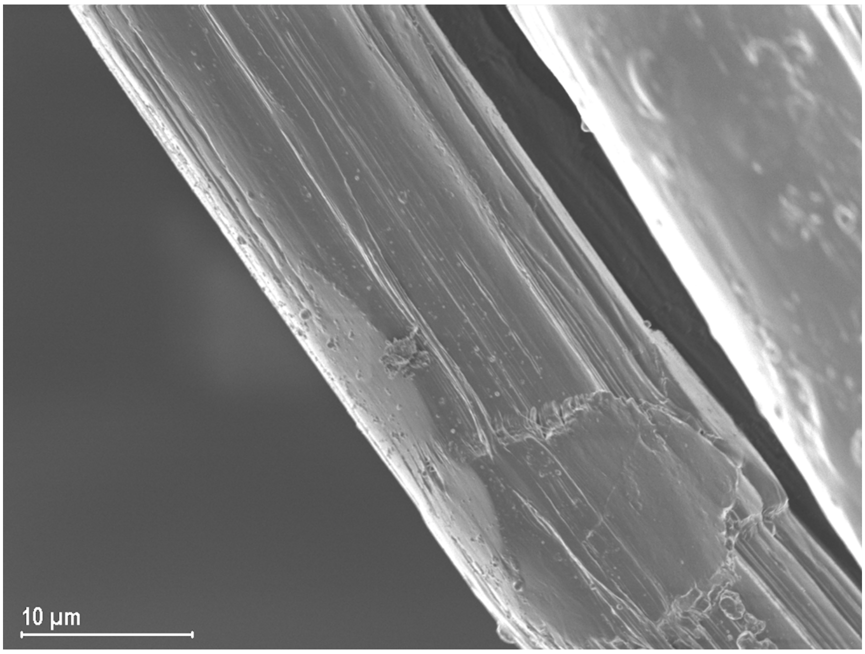

FIGURE 4.6: SEM image of the Dyneema, which shows fiber diameter about 20 μm.

4.2 Surface Chemistry

This section addresses the research topic **T1**, namely it gives some insights about the surface chemistry of polyethylene fabrics.

4.2.1 FTIR Measurememts

In general, polyethylene is a non polar molecule thus it presents hydrophobic properties [25]. Hydrophobic materials are not common in fabrics, since they are not comfortable for human body and they do not allow the spread of sweat within the cloth for its evaporation. In the textile industry it is common to apply plasma treatment to convert hydrophobic material into hydrophilic ones [25]; unfortunately this process requires expensive machinery.

In the case of woven PE and knitted PE to lower the production cost, it has been decided to exploit the high temperature reached during the extrusion of the single fibers to make them partially oxidised. The partial oxidation introduces polar bonds in the PE molecule, which enables the hydrophilicity of the material.

To assess the modification introduced during this process, the FTIR-ATR measurement has been used (Figure 4.7).

FIGURE 4.7: Particular of an FTIR machine (Thermo Electron Corporation, model Nicolet Continuum) equipped with a germanium crystal which is in direct contact with the fabric under testing.

The Attenuated Total Reflectance (ATR) is one of the most common technique among the Fourier Transform Infrared Reflectance (FTIR) methods to experimentally understand the structure of a tested material. In this technique, an IR beam is directed on a crystal, in our case germanium, which must have a refractive index higher than the material under testing, in our case polyethylene textiles. The beam, when reflected by the crystal, generates an evanescence wave that penetrates into the sampling material. By varying the wavelength of the input IR beam and analysing the intensity of the output wave, the main information about the structure can be identified.

The tests have been performed for all the PE fabrics for three different ageing of the material (Figure 4.8):

- New: benchmark material for polyethylene, just after surface oxidation treatment;
- Old, 5th cycle: material used for five cycles of wetting and natural drying. Here the material is only partially oxidised, since the usage destroys some polar bonds;
- Old, hand-washed: it is used as benchmark to characterise pure polyethylene fabrics before the oxidation treatment. The "hand-washing" protocol consists in rubbing by hand the "New" material with distilled water to eliminate the chemical bonds that have been introduced during the oxidation treatment.

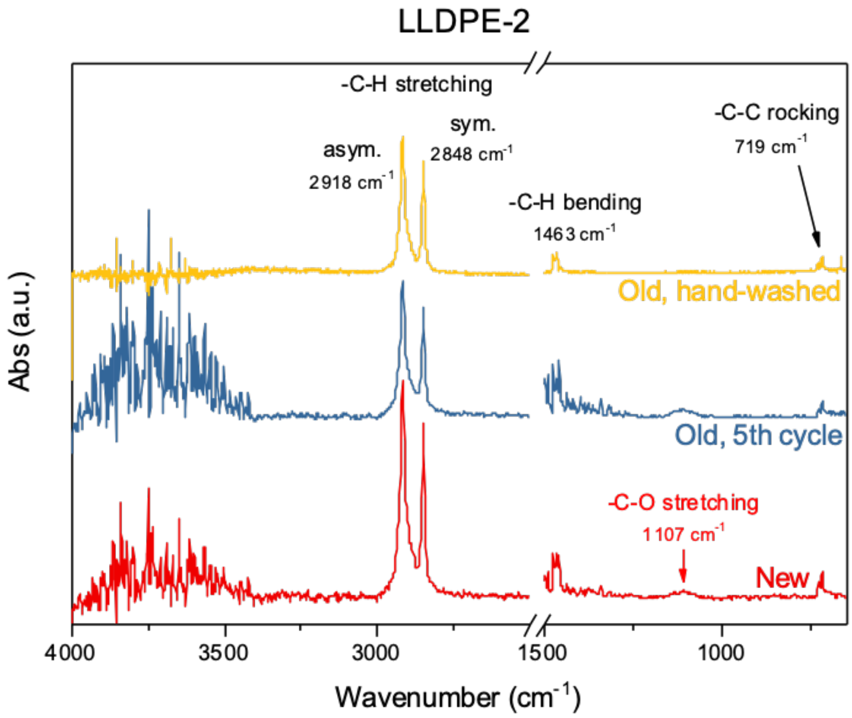

FIGURE 4.8: FTIR results obtained for a sample of knitted 2 polyethylene. Three samples of the same material with different usage have been tested: "New", "Old, 5th cycle", "Old, hand washed". Note that the noise between 3200 cm^{-1} and 4000 cm^{-1} is just due to the not perfect contact between crystal and fabric.

The three samples present the classic absorption peaks of polyethylene, namely the so called:

- asymmetric, at 2918 cm^{-1}
- symmetric, at 2848 cm^{-1}
- bending, at 1463 cm^{-1}
- rocking, at 719 cm^{-1}.

However, the "New" sample shows a singular peak at 1107 cm^{-1}, which is not present in pure polyethylene ("Old, hand washed") and is typical of carbon oxygen polar bonds $-C-O$.

4.2.2 Wettability

To verify that the presence of polar bonds $-C-O$ due to the oxidation treatment can change the hydrophilicity properties of the material, some wettability experiments have been performed (Figure 4.9).

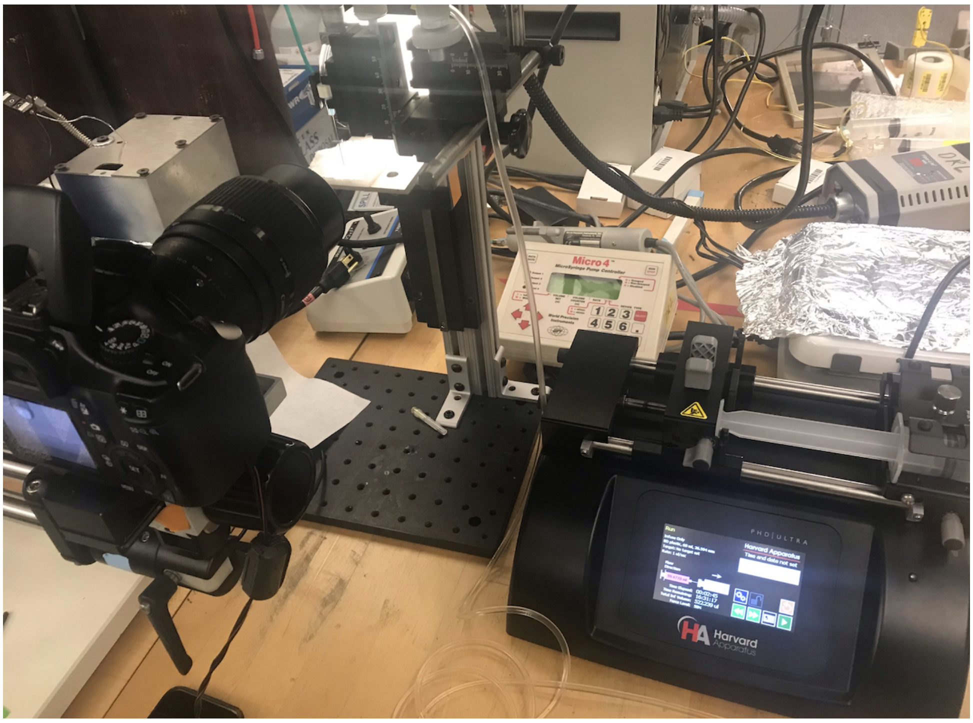

FIGURE 4.9: Experimental set up to perform wettability test: a syringe pump (Harvard Apparatus, model PHD ULTRA) is connected through a small pipe to a needle which provides small droplets of water on the surface of the fabric under testing.

The experimental set up consists in a syringe pump to feed a controlled flow rate of water through a small pipe, whose end is connected with a needle. The needle is placed vertically on top of a flat hydrophobic support, on which the fabric to test lays. The movement of the syringe pump allows to provide small droplets of water on the surface of the fabric, an high resolution camera is used to observe the motion of the droplet. These experiments are commonly used in the textile field to measure the dynamic contact angle [26]. Differently than in solid surface or hydrophobic membrane where the contact angle is static, for hydrophilic fabrics the contact angle changes in time due to capillary actions.

The test has been performed both for knitted and woven polyethylene samples in the "New" and "Old, 5th cycle" configurations. The results confirms that the new material presents strong hydrophilic properties, thus the contact angle after 1 s tends to zero due to capillary actions (Figure 4.10). On the other hand, in the old sample partially oxidised the spread of water is more slower, it takes 40 approximately, due to a little presence of $-C-O$ bonds (Figure 4.11).

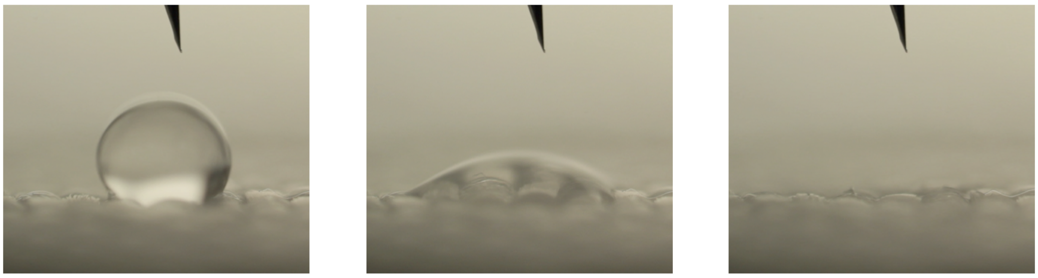

0 s 0.1 s 1 s

FIGURE 4.10: Example of wettability test for a new woven PE sample, the droplet of water due to capillary action spreads in less than 1 s into the fabric.

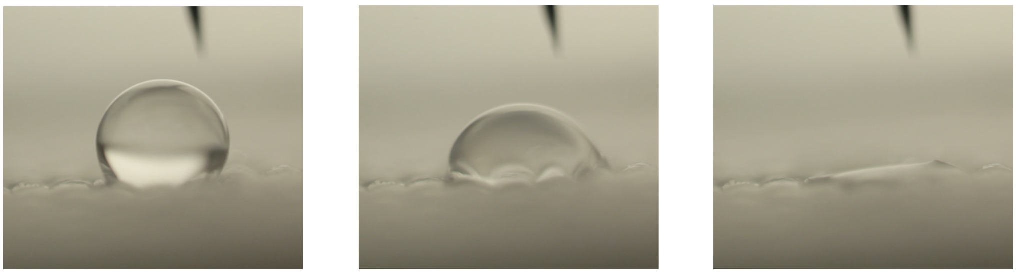

0 s 20 s 40 s

FIGURE 4.11: Example of wettability test for a old woven PE sample, in which the partial oxidation of the surface makes the droplet spread slower than in the new sample.

4.2.3 Wet - Dry Cycles

At present the oxidation treatment is not stable in time, meaning that after a certain number of washing cycles the fabrics come back to hydrophobic properties. To assess the durability of the oxidation process, some vertical imbibition tests have been performed and the heights reached in the different repetitions measured after two benchmark times: 5 and 10 minutes. After every repetition, the sample naturally dries at ambient temperature for 24 hours. Besides the woven and knitted PE samples also the commercial PE (Dyneema) has been tested.

The Dyneema sample show the fastest decrease of the hydrophilic property during the different repetitions (Figure 4.12 (b)): after the second wicking test both for 5 and 10 minutes, the height becomes a fourth of the initial one. In addition, after the fifth cycle, the material becomes completely hydrophobic with null wicking properties.

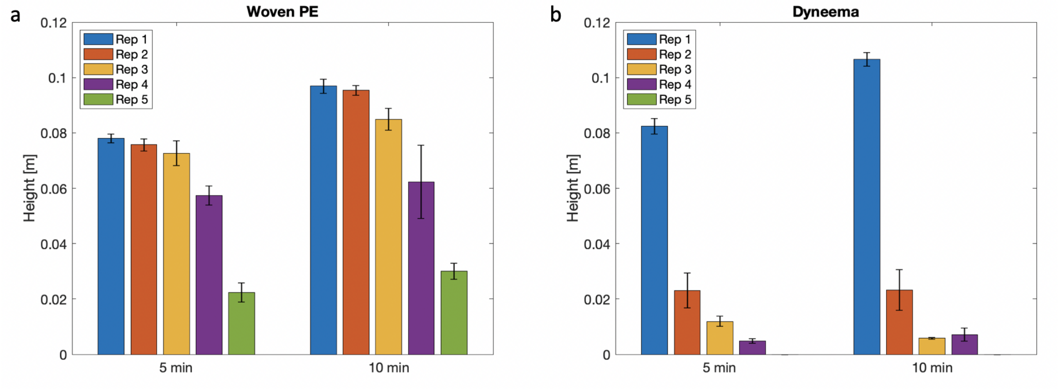

FIGURE 4.12: The plots report the height reached after 5 and 10 minutes during a vertical imbibition test up to the fifth cycle of drying. The Dyneema after the first washing cycle shows a rapid degradation of water transport properties becoming, after the fifth cycle, completely hydrophobic. The error bars are computed with equation 3.38.

The woven PE and knitted PE (1) show a more stable behaviour than Dyneema, but still the height reached after the fifth repetition is lower than the 50% of the initial one (Figure 4.12 (a) and 4.13 (a)).

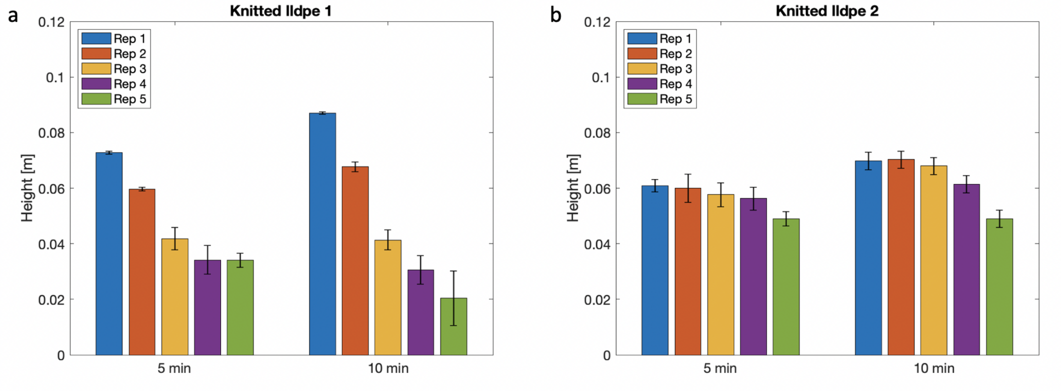

FIGURE 4.13: The plots report the height reached after 5 and 10 minutes during a vertical imbibition test up to the fifth cycle of drying: the knitted 2 sample is the one that shows the most constant results over the different drying cycles. The error bars are computed with equation 3.38.

The most promising results have been obtained with the second version of the knitted sample, where the height during the subsequent repetitions is much more stable (Figure 4.13 (b)). Future works will concentrate on the surface treatment process to make the hydrophilic property more stable in time in order to assure more stable comfort for the human body.

4.3 Water Transport Properties

This section addresses research topic **T2**, namely it gives quantitative results about the parameters presented in section 3.2 to describe the water transport within the fabrics.

4.3.1 Wicking Effective Porosity

The wicking effective porosity has been computed thanks to the procedure presented in section 3.2.1. The plots that correlate the wicking height $h_{\Delta t}$ and the imbibiton mass $m_{\Delta t}$ are presented below.

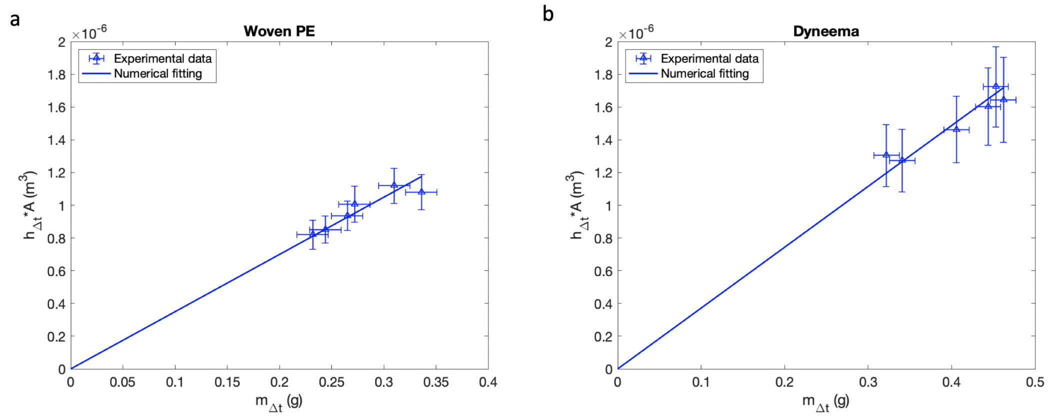

FIGURE 4.14: The plots report the experimental vertical imbibition height as function of the imbibition mass for woven PE (a) and Dyneema (b) fabrics. The numerical fitting is obtained thanks to equation 3.32 and the uncertainty is computed based on equation 3.40.

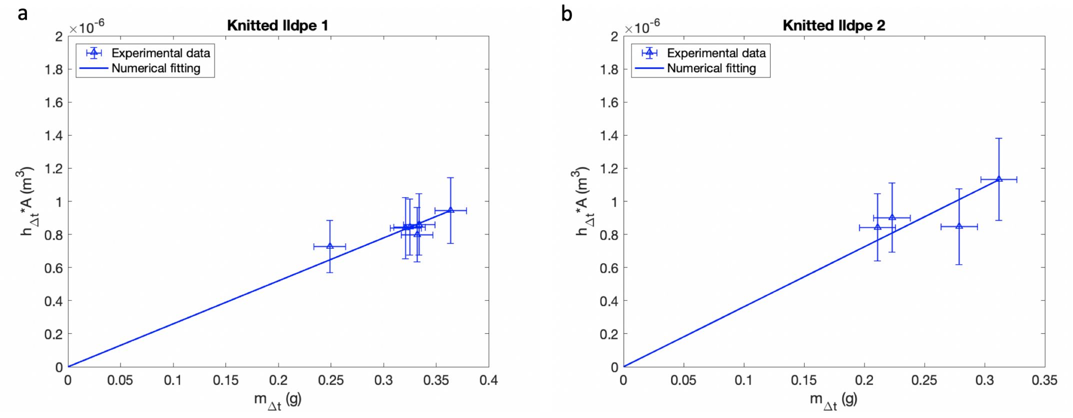

FIGURE 4.15: The plots report the experimental vertical imbibition height as function of the imbibition mass for knitted PE version 1 (a) and knitted PE version 2 (b) fabrics. The numerical fitting is obtained thanks to equation 3.32 and the uncertainty is computed based on equation 3.40.

By fitting the slope of the these curves (see equation 3.32), the effective wicking porosity ϕ_e with its expanded uncertainty (see section 3.2.4) can be obtained:

Table 3. Wicking effective porosity ϕ_e

Material	ϕ_e	U_{ϕ_e}
Woven PE	0.29	0.02
Dyneema	0.27	0.05
Knitted PE 1	0.39	0.12
Knitted PE 2	0.33	1e-8

4.3.2 Capillary pressure

The capillary pressure can be computed through the measurement of the maximum capillary height from Jurin's law (see section 3.2.2). The values of the maximum capillary height obtained from vertical imbibition tests are the following:

Table 4. Maximum capillary height h_{max}

Material	h_{max} (cm)	$U_{h_{max}} \cdot 10^{-3}$ (cm)
Woven PE	13.8	8.4
Dyneema	14.5	5.3
Knitted PE 1	16.4	6.1
Knitted PE 2	15.3	5.0

Hence, the value of capillary pressure p_c and the expanded uncertainty U_{p_c} are computed thanks to equation 3.33, with results shown in Table 4:

Table 5. Capillary pressure p_c

Material	p_c (Pa)	U_{p_c} (Pa)
Woven PE	1353.8	0.82
Dyneema	1422.5	0.5
Knitted PE 1	1608.8	0.6
Knitted PE 2	1500.9	0.5

The knitted PE samples perform better than Dyneema and woven PE in term of wicking distance, namely they can reach a larger maximum wicking distance, which can potentially enhance a faster evaporation of the sweat towards the environment.

4.3.3 Permeability

The general method to compute the permeability is presented in section 3.2.3. The hypothesis to use the Lucas-Washburn model (see equation 3.28) is that the material is perfectly rigid, meaning that it does not undergoes any mechanical deformations.

This assumption turns out to hold only for woven PE and Dyneema: in these cases the value of permeability computed from horizontal imbibition tests, can be used in the vertical model in equation 3.27 to retrieve the experimental imbibition height obtained in presence of gravity (Figure 4.16).

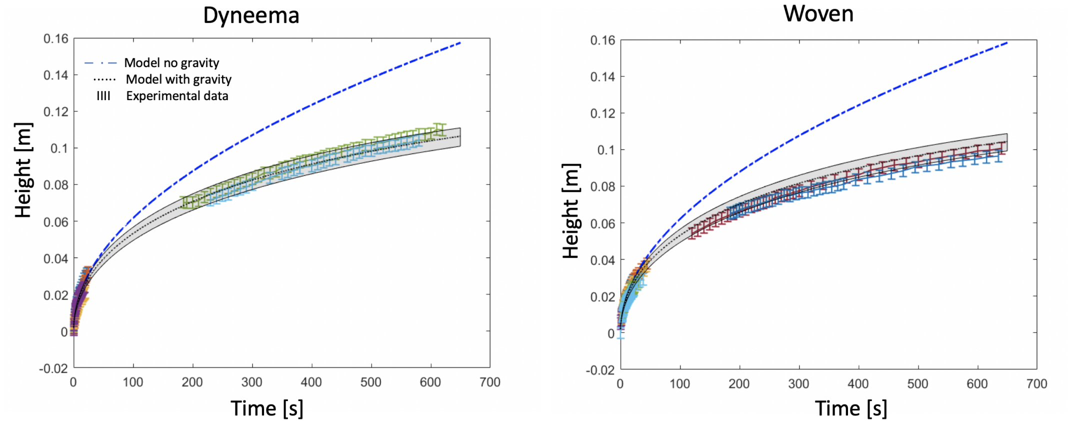

FIGURE 4.16: By knowing the porosity and the capillary pressure, horizontal imbibition tests are performed to fit the permeability, in this case the experimental heights correspond to the ones from 0 to 50 s, approximately. This value is used as input for the model in presence of gravity to recover the experimental vertical data whose heights correspond to the interval 200 s to 600 s, approximately. In this case, since the two materials are perfectly rigid, the gravity model with constant parameters can be used. The grey span is obtained considering the expanded uncertainty on the value of porosity and capillary pressure in the model with gravity. Here, the "Model no gravity" and "Model with gravity" are based on equations 3.28 and 3.27, respectively.

On the contrary, in the case of knitted PE samples, the materials show high deformations due to the weight of the absorbed water. Hence, a model that takes into account the shrinkage of the material has been introduced to retrieve the experimental vertical heights that, with a constant parameters model 3.28, can not be predicted (Figure 4.17).

An exponential correction for the permeability that allows to consider the change in the material properties during time has been introduced. The latter accounts for the fact that the shrinkage of the material causes a decrease in the pore radius and a subsequent increase of the viscous losses. The value of K_h obtained from the horizontal tests has been corrected by introducing two constant A, B proper of each material. The first one is proportional to the rate of deformation of the material, while the second one gives information about its stationary behaviour:

$$K = K_h\Big((1 - B) \cdot e^{-At} + B\Big) \tag{4.1}$$

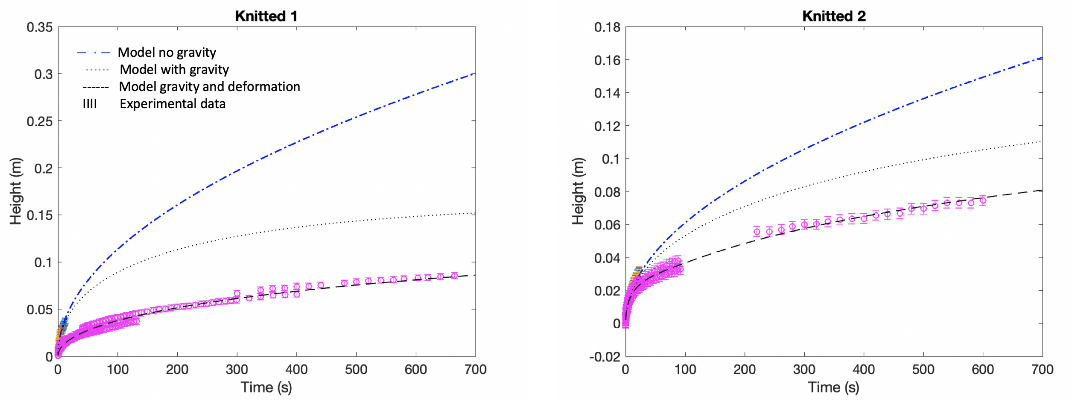

FIGURE 4.17: Introduction of model for permeability that accounts for the deformation of the material during time. The value of permeability K_h is obtained from horizontal imbibition tests using the "Model no gravity" through equation 3.28, whose heights correspond to the interval of time 0-30 s, approximately. When considering vertical imbibition tests, whose experimental heights correspond to the time interval 30-600 s, the "Model with gravity" based on equation 3.27 with the value of permeability K_h can not be used to recover the experimental data. In this case another model that takes into consideration the deformation of the fabric must be introduced: "Model gravity and deformation", according to equation 4.1.

The values obtained in the horizontal tests and their expanded uncertainty are reported below:

Table 6. Permeability in horizontal tests K_h

Material	$K_h \cdot 10^{-12}$ (m^2)	U_{K_h} (m^2)
Woven PE	3.9	0.01
Dyneema	3.7	0.02
Knitted PE 1	15.6	0.02
Knitted PE 2	34.7	0.001

and the corrective dimensionless parameters for the model accounting also for the mechanical deformation are:

Table 7. Correction parameters A, B

Material	A	B
Knitted PE 1	$+\infty$	0.13
Knitted PE 2	$2.2 \cdot 10^{-2}$	0.35

The $+\infty$ value for knitted 1 PE sample means that the deformation is so fast that the material in vertical imbibition test can be modelled with a constant permeability value of:

$$K = K_h \cdot B \tag{4.2}$$

The different rigidity of the two materials can be easily shown by comparing the imbibition heights in horizontal and vertical tests. In fact, the two materials show different behaviours during horizontal wicking (Figure 4.18 - "Horizontal model"), while in vertical tests they present similar performances (Figure 4.18 - "Gravity model with deformation"). This change from different performances in horizontal tests to similar ones in the vertical case, demonstrates the different rigidity of the material.

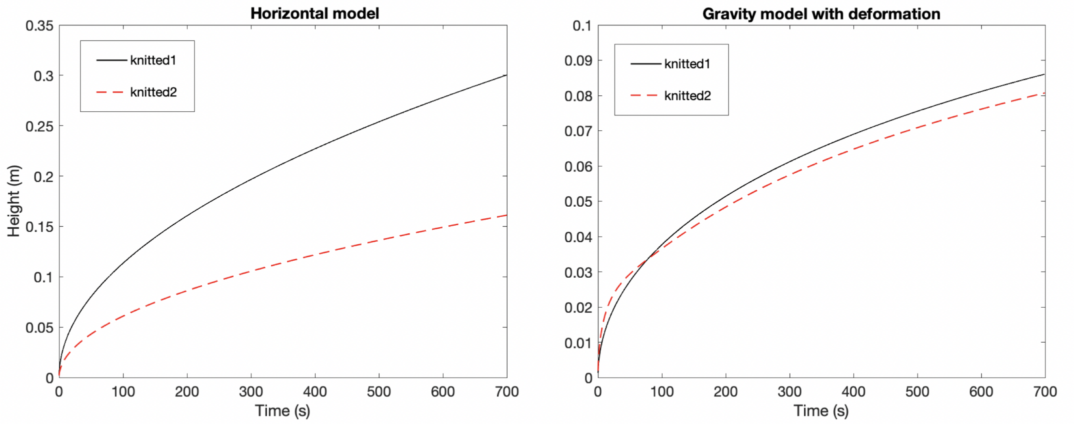

FIGURE 4.18: The comparison between horizontal and vertical tests clarifies the different rigidity of the materials that produce different values for the constant A, B. The two materials show different performances during horizontal wicking, while their different rigidity implies that they present similar performances in vertical tests. The "Horizontal model" and "Gravity model with deformation" are based on equations 3.28 and 4.1.

4.4 Indoor and Outdoor Thermal Performances

This section addresses the research topic **T3**, specifically it shows the thermal effects of different textiles on the temperature of the human skin, as described in section 2.4.4.

Recalling that, for daytime sub - ambient radiative cooling applications the difference between the temperature of the bare skin and the covered skin should be minimised, the results for indoor (Figure 4.19) and outdoor (Figure 4.20) conditions are reported below.

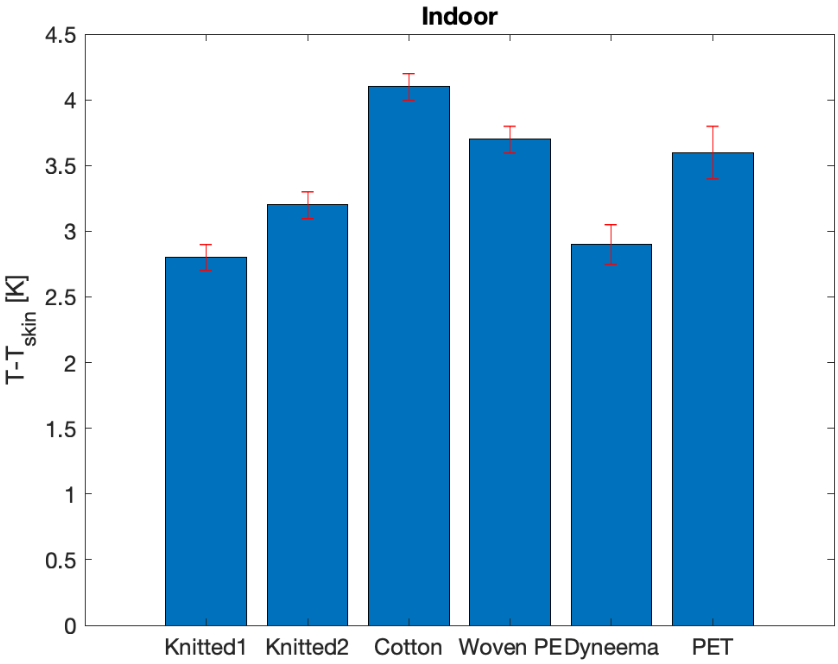

FIGURE 4.19: The plots shows the difference between the temperature of the skin covered with a fabric T and the bare skin T_{skin} in indoor conditions. The knitted samples show a lower temperature difference with respect to common garment, e.g. cotton, and sportswear made of polyester (PET).The error bars are computed with equation 3.36 considering 60 min of steady state for each material.

For what concerns indoor conditions, the most promising materials are knitted PE 1 and knitted PE 2, which show better thermal performances than common material, i.e cotton, but also of technical material such as polyester (PET). Specifically, knitted PE 1 shows a 1.3^oC decrease in temperature and 0.9^oC in the case of knitted PE 2 with respect to cotton, which is used as benchmark material. A similar experimental set up is used also by [9], in this case the polyethylene fabrics are coated with polydopamine, then a second layer of cotton is introduced to form the so called "PDA-nanoPE-mesh". In the latter case, the difference between the covered skin and the bare skin present better results for indoor conditions, e.g. a decrease of 2^oC with respect to cotton. It is worthy to underline that the "PDA-nanoPE-mesh" solution shows better thermal performances than the knitted PE samples, but the structure is more complex, since a double layer configuration is used to give hydrophilic properties to the material.

For what concerns outdoor experiments, similar results are obtained also in this conditions, where the optimal performances of knitted PE samples are confirmed over the other materials, e.g cotton and polyester (PET).

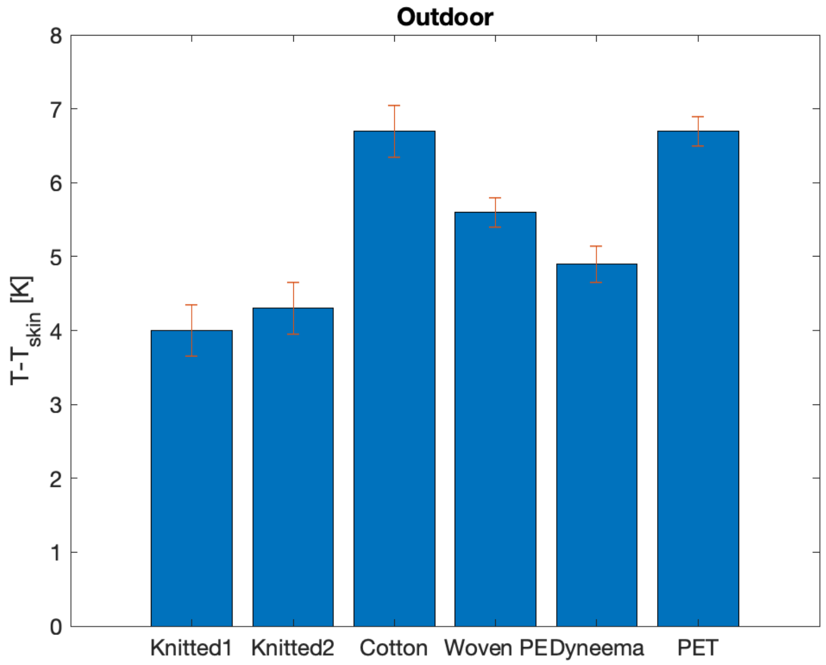

FIGURE 4.20: The plots shows the difference between the temperature of the skin covered with a fabric T and the bare skin T_{skin} in outdoor conditions.The error bars are computed with equation 3.36 considering 60 min of steady state for each material.

Concluding, [7] predicts that a decrease of 1-2 ^oC in the human skin temperature can potentially diminish the use of air conditioning by 30 %, which could save a significant amount of money and decrease the CO_2 emissions.

Chapter 5

Conclusions

This chapter summarises the work presented in the thesis, finally a graphical comparison of the performances of different fabrics is proposed.

Concerning the surface chemistry, the hydrophilicity of the testing materials is guaranteed thanks to a partial oxidation of the surface during the production of the fibers. This process allows to lower the production cost with respect to apply plasma treatment [25] or a multi layered structure [9].

A model for predicting the water mass transport has been introduced, specifically for the samples with high rigidity, e.g. woven PE and Dyneema, a classical imbibition model can be applied (see equations 3.27 and 3.28). On the contrary, for the materials that show higher mechanical deformations during the imbibition process due to the weight of the water, a correction for the permeability has been introduced (see equation 4.1), in order to retrieve the experimental data.

Finally, an experimental set up to test the thermal effects of different garments on the human skin has been introduced.

By comparing the main parameters that has been measured in the thesis (see Figure 5.1):

- Porosity,
- Maximum capillary height,
- Permeability,
- Indoor temperature difference with respect to cotton (*Dt Indoor*), which is computed from figure 4.19 by subtracting: $(T_{cotton} - T_{skin}) - (T_{PE} - T_{skin})$,
- Outdoor temperature difference with respect to cotton (*Dt Outdoor*), which is computed from figure 4.20 by subtracting: $(T_{cotton} - T_{skin}) - (T_{PE} - T_{skin})$,
- Wicking distance in vertical imbibition test at 10 min, after the $5th$ washing cycle,

it turns out that the knitted PE samples perform better in nearly all the parameters. Specifically, they guarantee a faster spread of the water, e.g. higher permeability, that allows the sweat to rapidly move through the fabric, thus enhancing its evaporation and a better comfort.

Concerning thermal comfort, they show positive temperature difference with respect to cotton fabrics: both in indoor and outdoor conditions, $Dt\ Indoor$ and $Dt\ outdoor$, respectively. This implies that when the human body is covered by knitted PE fabrics, the temperature of the skin is lower than when using common cotton garments.

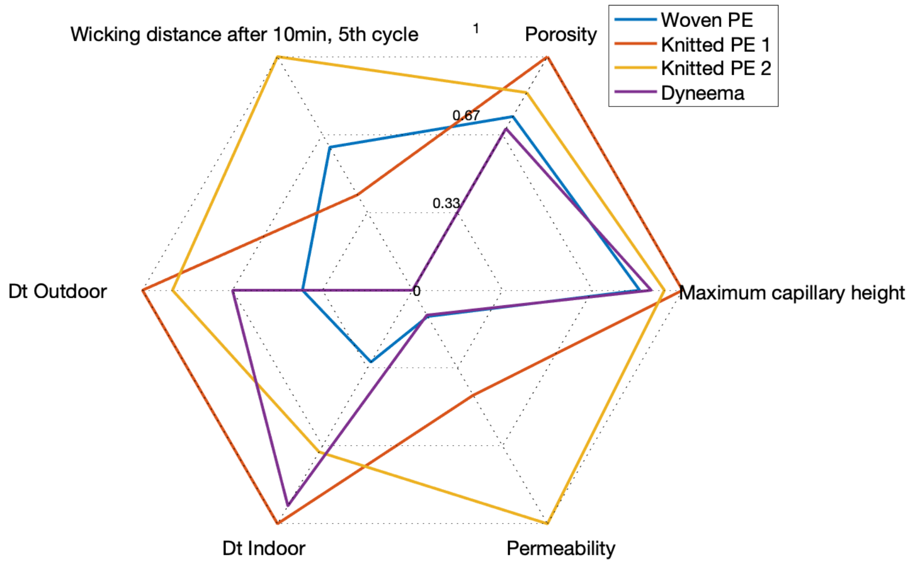

FIGURE 5.1: Radar plot of the main parameters that characterise the wicking and thermal properties of polyethylene fabrics. All the parameters have been adimensionalized considering the maximum value of each parameters among the different materials.

In the future, further works will concentrate on optimising the oxidation treatment to make it more stable in time. In addition, the effect of evaporation will be coupled to the radiative thermal effect on the skin temperature. The ultimate goal is to find the optimal structural parameters of the fabric, which allow to assure the best comfort possible to the human body for cooling applications.

Bibliography

[1] *Thermal comfort conditions*. ASHRAE standard (1966).

[2] https://www.iea.org/topics/energyefficiency/buildings/cooling/.

[3] E.W. Shaw. “Thermal Comfort: analysis and applications in environmental engineering, by P. O. Fanger. 244 pp. DANISH TECHNICAL PRESS. Copenhagen, Denmark, 1970. Danish Kr. 76, 50”. In: *Royal Society of Health Journal* 92.3 (1972), pp. 164–164.

[4] Motahareh Mokhtari Yazdi and Mohammad Sheikhzadeh. “Personal cooling garments: a review”. In: *The Journal of The Textile Institute* 105.12 (2014), pp. 1231–1250.

[5] *Infrared transparent visible opaque fabrics*. Gang Chen, Jonathan K. Tong, Svetlana Boriskina, Xiaopeng Huang, James Loomis, Yanfei Xu; US Patent 2015, 050720.

[6] Jonathan K. Tong et al. “Infrared-Transparent Visible-Opaque Fabrics for Wearable Personal Thermal Management”. In: *ACS Photonics* 2.6 (2015), pp. 769–778.

[7] Svetlana V. Boriskina. “An ode to polyethylene”. In: *MRS Energy amp; Sustainability* 6 (2019), E14. DOI: 10.1557/mre.2019.15.

[8] Chenxing Wang et al. “Carbon footprint of textile throughout its life cycle: a case study of Chinese cotton shirts”. In: *Journal of Cleaner Production* 108 (2015), pp. 464–475.

[9] Po-Chun Hsu et al. “Radiative human body cooling by nanoporous polyethylene textile”. In: *Science* 353.6303 (2016), pp. 1019–1023.

[10] Mark Fox. *Optical Properties of Solids*. Oxford University Press Inc., New York, 2001.

[11] Donald R. Huffman Craig F. Bohren. *Absorption and Scattering of Light by Small Particles*. John Wiley Sons, Inc., 1983.

[12] Romano Borchiellini Adriano Sciacovelli Vittorio Verda. *Numerical design of thermal systems*. CLUT, 2013.

[13] Helmut Schmitz and H. Bousack. “Modelling a Historic Oil-Tank Fire Allows an Estimation of the Sensitivity of the Infrared Receptors in Pyrophilous Melanophila Beetles”. In: *PloS one* 7 (May 2012), e37627. DOI: 10.1371/journal.pone.0037627.

[14] Bin Zhao et al. “Radiative cooling: A review of fundamentals, materials, applications, and prospects”. In: *Applied Energy* 236.C (2019), pp. 489–513.

[15] J. Steketee. “Spectral Emissivity of Skin and Pericardium”. In: *Physics in Medicine Biology* 18.5 (1973), pp. 686–694.

[16] Hardy JD. “The Radiation Heat from the Human Body : An Instrument for Measuring the Radiation and Surface Temperature of the Skin”. In: *The Journal of Clinical Investigation* 13.4 (1934), pp. 593–604.

[17] T Togawa. “Non-contact skin emissivity: measurement from reflectance using step change in ambient radiation temperature”. In: *Clinical Physics and Physiological Measurement* 10.1 (Feb. 1989), pp. 39–48.

[18] Francisco J. Sanchez-Marin, Sergio Calixto-Carrera, and Carlos Villaseñor-Mora. “Novel approach to assess the emissivity of the human skin”. In: *Journal of Biomedical Optics* 14.2 (2009), pp. 1–6.

[19] Aaswath Raman et al. “Passive radiative cooling below ambient air temperature under direct sunlight”. In: *Nature* 515 (2014), pp. 540–544.

[20] Aden B. Meinel. *Applied Solar Energy: An Introduction*. Addison-Wesley, 1976.

[21] Adrian Bejan Donald A. Nield. *Convection in Porous Media*. Springer International Publishing, 2017.

[22] M. Amin F. Zarandi, Krishna M. Pillai, and Adam S. Kimmel. “Spontaneous imbibition of liquids in glass-fiber wicks. Part I: Usefulness of a sharp-front approach”. In: *AIChE Journal* 64.1 (2018), pp. 294–305.

[23] Nicolas Fries et al. “The effect of evaporation on the wicking of liquids into a metallic weave”. In: *Journal of colloid and interface science* 321 (June 2008), pp. 118–29.

[24] Barry N. Taylor and Chris E. Kuyatt. *Guidelines for Evaluating and Expressing the Uncertainty of NIST Measurement Results*. NIST Technical Note 1297, 1994.

[25] Joanna Izdebska. *Printing on Polymers. Fundamentals and Applications*. Elsevier, 2016.

[26] Shuhui Li et al. “A review on special wettability textiles: theoretical models fabrication technologies and multifunctional applications”. In: *J. Mater. Chem. A* 5 (1 2017), pp. 31–55.